East European Journal of Physics. 3. 325-346 (2026)
DOI:10.26565/2312-4334-2026-3-29 ISSN 2312-4334

MULTIFUNCTIONAL BULK METALLIC GLASS: AN AB INITIO STUDY ON $Pd_{39}Ni_{10}Cu_{30}P_{21}$ FOR ENHANCED MECHANICAL STRENGTH AND OPTICAL SHIELDING

Sangita Gupta[1], Amit Kumar Chaubey[2], Sarita Chaudhary[3], Kapil Bhardwaj[4], Abhay P. Srivastava[5]*
[1]*Department of Chemistry, Poornima University, Jaipur, Rajasthan, India*
[2]*Department of Applied Science and Humanities, United College of Engineering and Research, Prayagraj, (UP), India*
[3]*Department of Chemistry, Vivekanand Global University, Jaipur, Rajasthan, India*
[4]*Department of Computer Science and Engineering, Chandigarh University, Mohali, Punjab, India*
[5]*Department of Applied Science and Humanities, Bansal Institute of Engineering and Technology, Lucknow (UP), India*
**Corresponding Author email ID: abhay.srivastava831@gmail.com*
Received April 20, 2026; revised June 17, 2026; accepted June 26, 2026

Bulk metallic glasses (BMGs) are a type of solid material with amorphous atomic structures that exhibit favorable mechanical, thermal, and functional properties. This study presents the attributes of the glass, examining first-principles details of the $Pd_{39}Ni_{10}Cu_{30}P_{21}$ bulk metallic glass structure, its elastic properties, thermodynamics, and electronic–optical performance. Density functional theory calculations were performed for a comparison with the amorphous atomic configuration and energy–volume relation through a third-order Birch–Murnaghan equation of state. The very high bulk modulus of approximately 159 GPa and >6 pressure derivatives demonstrated uniformity, resistance, and strong pressure strengthening. All three elastic moduli, Poisson's ratio, and Pugh's criterion are constantly demonstrating ductile mechanical response dependent on shear transformation zone–mediated plasticity. The results of the thermophysical examination show stable anharmonic lattice behavior, a Debye temperature of approximately 395 K, and favorable thermal expansion, indicating good predictability of the thermomechanical response. Electronic studies revealed a very metallic phase with low pseudogap around the Fermi level—mainly the hybridization between transition metal d-states and phosphorus p-states into a stable, amorphous phase. Optical spectra that contain a wide band, excellent reflectivity at low photon energies, and an isotropic optical response are typical of metallic glasses. In conclusion, these results prove $Pd_{39}Ni_{10}Cu_{30}P_{21}$ as a highly mechanically stable material for progress in various mechanical, optical, and energy applications in a lightweight frame.
Keywords: *Bulk metallic glass; Density functional theory; Equation of state; Mechanical and thermophysical properties; Electronic structure; Optical shielding materials*

INTRODUCTION

Over the years, bulk metallic glasses received extensive scientific and technological interest owing to their unique atomic structures and property mixes that are not achievable in traditional crystalline alloys [1]. In contrast to crystalline metals, which possess long-range periodicity and dislocation-mediated plasticity, BMGs exhibit disordered atomic arrangements with pronounced short- and medium-range order [2]. Structural disorder, which suppresses crystallization and dislocation motion, leads to ultrahigh strength, large elastic limits, excellent corrosion resistance, and unique electronic and optical responses [3].

Among the BMG systems, Pd-based alloys are most popular due to their excellent glass-forming capability, thermal stability, and ductility, and represent a model system for understanding the structure–property relationships of metallic glasses [4]. The $Pd_{39}Ni_{10}Cu_{30}P_{21}$ alloy is a conventional Pd-based bulk metallic glass characterized by high atomic density, powerful heteroatomic bonding, and a wide supercooled liquid region [5]. It is important that phosphorus is included to stabilize the amorphous structure, as it provides chemical short-range order through energetically favorable Pd–P and Cu–P bonds that frustrate long-range crystalline ordering [6-7].

These characteristics not only maximize glass-forming capability but also influence mechanical deformation processes controlled by localized atomic reorganization (shear transformation zones), rather than lattice imperfections [8-9]. Despite extensive experimental experience with Pd-based BMG, a single first-principles description that links atomic-scale structure to mechanical, thermodynamic, electronic, and optical behavior is scarce [10-11].

Specifically, the joint influence of dense random packing, polyhedral short-range order, and electronic hybridization on pressure resistance, ductility, thermal response, and optical loss is relevant to predictive materials design [12]. Density functional theory provides a robust framework for addressing these questions by enabling atomistic modeling of amorphous structures and the quantitative assessment of intrinsic properties. In this work, a comprehensive ab initio characterization of $Pd_{39}Ni_{10}Cu_{30}P_{21}$ in bulk metallic glass form is executed. Structural stability is checked through energy–volume analysis and equation-of-state fitting, elastic constants and moduli are calculated to evaluate mechanical stiffness and ductility [13-15].

Lattice behavior and thermal reliability are characterized by thermophysical properties, such as the Debye temperature, Grüneisen parameter, and thermal expansion [16-17]. Moreover, the electronic density of states, dielectric response, optical conductivity, and related spectra are investigated to deduce metallic optical behavior and a broadband

Cite as: S. Gupta, A.K. Chaubey, S. Chaudhary, K. Bhardwaj, A.P. Srivastava, East Eur. J. Phys. 3, 325 (2026), https://doi.org/10.26565/2312-4334-2026-3-29

energy-dissipation mechanism. The aims of the study are to correlate atomic-scale structure with macroscopic properties to acquire a comprehensive physical understanding of $Pd_{39}Ni_{10}Cu_{30}P_{21}$ and to demonstrate its potential for high-performance multifunctional applications [18-20].

In this study, the first principles framework has been used to investigate the intrinsic structure–property relationships of the $Pd_{39}Ni_{10}Cu_{30}P_{21}$ bulk metallic glass through the atomic and electronic scales. In contrast, periodicity in crystalline materials characterizes mechanical and optical behavior, but the multifunctional properties of metallic glasses are determined by dense random packing, chemical short-range order, and disorder-broadened electronic states. The current endeavor seeks to address this issue by linking amorphous atomic topology to elastic response, thermodynamic stability, electronic structure, and broadband optical shielding in a unified density functional theory (DFT) scheme.

The focus is on the application of pressure resistance, shear-transformation-zone-mediated ductility, and electronic hybridization together in isotropic optical absorption, reflectivity at low photon energies, and efficiency of electromagnetic energy dissipation. On the basis of this integrated investigation, $Pd_{39}Ni_{10}Cu_{30}P_{21}$ is shown to be a mechanically robust and optically effective material, ready for next-generation structural, photothermal, and electromagnetic shielding applications.

COMPUTATIONAL METHODOLOGY

All first-principles calculations were carried out within the framework of Density Functional Theory (DFT), where the interacting many-electron problem is mapped onto an equivalent system of non-interacting electrons moving in an effective potential. According to the Kohn–Sham formalism, the total ground-state energy of the system is expressed as [21-22]:

$$E_{tot}[\rho(r)] = T_s[\rho] + E_{ext}[\rho] + E_H[\rho] + E_{xc}[\rho], \tag{1}$$

where T_s is the kinetic energy of non-interacting electrons, E_{ext} is the electron–ion interaction energy, E_H is the Hartree electrostatic energy, and E_{xc} is the exchange–correlation functional accounting for many-body effects beyond classical electrostatics.

The exchange–correlation energy was treated using the generalized gradient approximation (GGA) in the Perdew–Burke–Ernzerhof (PBE) formulation, which provides an improved description of metallic bonding and pressure-dependent properties compared to the local density approximation [23].

Since bulk metallic glasses lack long-range translational symmetry, sampling in the Brillouin zone must be balanced against the need to capture the electronic structure and the computational cost. For this purpose, the Brillouin zone was sampled according to the Monkhorst–Pack scheme to produce a uniform grid of k-points in reciprocal space by relation. As the long-range translational symmetry in metallic glasses is nonexistent, the sampling for the Brillouin zone needs to be considered for a high degree of precision to acquire the full electronic structure and computation time. We used the Monkhorst–Pack scheme for Brillouin zone sampling in this study. This approach is aimed at ensuring a consistent grid of k-points in reciprocal space, with a particular mathematical relation, to achieve maximum precision and computational efficiency [24-25].

$$\vec{k}_{n_1 n_2 n_3} = \sum_{i=1}^{3} \frac{2n_i - N_i - 1}{2N_i} \vec{b_i} \tag{2}$$

where N_i is the number of divisions along the reciprocal lattice vector $\vec{b_i}$, and $n_i = 1,2, \ldots, N_i$.

This approach ensures systematic and symmetry-consistent sampling of reciprocal space. In the case of the large amorphous supercell used in this work, the electronic states are very localized in real space and reflect little dispersion in reciprocal space. As a result, Γ-point (1×1×1 Monkhorst–Pack) sampling was used, already proven adequate for metallic glass systems with larger unit cells. Convergence analysis showed that the total energy, density of states near the Fermi level and optical response functions of the data from increasing k-point density were little changed, providing evidence for the accuracy of Γ-point sampling in the current amorphous arrangement [26-27].

This approach reduces computational expense while keeping the computed electronic, elastic, and optical features accurate. Furthermore, Γ-point sampling is especially suitable for the evaluation of isotropic optical properties because it can refrain from leading to an artificial directional bias in sparse but anisotropic k-point grids. Therefore, the application of the Monkhorst–Pack k-space strategy provides a physically appropriate description of the disorder-broadened electronic structure and hence the broadband optical shielding performance of $Pd_{39}Ni_{10}Cu_{30}P_{21}$ [28-29].

Construction and Optimization of the Amorphous Structure:

The amorphous atomic configuration of $Pd_{39}Ni_{10}Cu_{30}P_{21}$ was generated using a large periodic supercell with randomly distributed atoms respecting the experimental stoichiometry. Structural relaxation was performed using a conjugate-gradient algorithm until the Hellmann–Feynman forces on each atom were less than 10^{-3} eV $Å^{-1}$ and the total energy convergence reached 10^{-6} eV [30]

Because bulk metallic glasses lack translational symmetry, Γ-point sampling of the Brillouin zone was adopted, which is sufficient for large amorphous supercells. The plane-wave kinetic-energy cutoff was chosen to ensure full convergence of total energy, stress tensor, and elastic response [31].

***Energy–Volume Relation and Equation of State**:*

To evaluate structural stability under compression, total energies were calculated for a series of uniformly compressed and expanded volumes around equilibrium. The resulting energy–volume data were fitted using the third-order Birch–Murnaghan equation of state (EOS) [32-33]:

$$E(V) = E_0 + \frac{9B_0V_0}{16}\left\{\left[\left(\frac{V}{V_0}\right)^{-2/3} - 1\right]^3 K_0' + \left[\left(\frac{V}{V_0}\right)^{-2/3} - 1\right]^2 \left[6 - 4\left(\frac{V}{V_0}\right)^{-2/3}\right]\right\} \tag{3}$$

where E_0 is the equilibrium energy, V_0 the equilibrium volume, B_0 the bulk modulus, and B_0' its pressure derivative. The corresponding pressure–volume relation is obtained as [34-35]

$$P(V) = \frac{3K_0}{2}\left[\left(\frac{V}{V_0}\right)^{-\frac{7}{3}} - \left(\frac{V}{V_0}\right)^{-\frac{5}{3}}\right]\left[1 - \frac{3\left(4 - K_0'\right)}{4}\left\{\left(\frac{V}{V_0}\right)^{-\frac{2}{3}} - 1\right\}\right] \tag{4}$$

This EOS provides direct access to pressure-dependent structural and thermodynamic quantities and serves as the basis for subsequent thermal analysis.

Elastic Constants and Mechanical Moduli:

The elastic stiffness constants C_{ij} were obtained using the stress–strain method, in which small finite deformations were applied to the optimized structure and the resulting stress response was computed. For an isotropic amorphous solid, the bulk modulus B and shear modulus G were derived as [36-37]

$$B = \frac{C_{11} + 2C_{12}}{3},\ G = \frac{C_{11} - C_{12} + 3C_{44}}{5}. \tag{5}$$

The Young's modulus $E$and Poisson's ratio νwere then obtained from

$$E = \frac{9KG}{3K + G} \tag{6}$$

$$\nu = \frac{3K - 2G}{2(3K + G)} \tag{7}$$

The ductile or brittle nature of the metallic glass was assessed using Pugh's ratio:

$$\frac{B}{G} > 1.75 \Rightarrow \text{ ductile behavior} \tag{8}$$

Thermophysical Properties:

The sound velocities were calculated from the elastic moduli and density ρ as [38-39]

$$v_l = \sqrt{\frac{3B + 4G}{3\rho}} \text{ and } v_t = \sqrt{\frac{G}{\rho}} \tag{9}$$

The average sound velocity is [38-39]

$$v_m = \left[\frac{1}{3}\left(\frac{2}{v_t^3} + \frac{1}{v_l^3}\right)\right]^{-1/3} \tag{10}$$

Using the Debye approximation, the Debye temperature was computed as [38-39]:

$$\theta_d = \frac{h}{k_B}\left(\frac{3n}{4\pi V}\right)^{1/3} v_m \tag{11}$$

where n is the number of atoms per unit cell, $V$the molar volume, hPlanck's constant, and k_BBoltzmann's constant.

The Grüneisen parameter γ, describing lattice anharmonicity, was estimated as [38-39]:

$$\gamma = \frac{3\alpha BV}{C_V} \tag{12}$$

where α is the volumetric thermal expansion coefficient and $C_V$the constant-volume heat capacity.

Electronic Structure Calculations:

The electronic band structure and density of states (DOS) were calculated from the converged Kohn–Sham eigenvalues. The total DOS is defined as [40]:

$$D(E) = \sum_{n.k} \delta(E - E_{n,k}) \tag{13}$$

Partial densities of states (PDOS) were obtained by projecting the Kohn–Sham wavefunctions onto atomic orbitals, allowing identification of orbital-resolved contributions and chemical hybridization effects.

Optical Properties:

The frequency-dependent complex dielectric function was calculated as [41-42]

$$\varepsilon(\omega) = \varepsilon_1(\omega) + i\varepsilon_2(\omega) \tag{14}$$

The imaginary part was obtained from interband transitions:

$$\varepsilon_2^{\alpha\beta}(\omega) = \frac{4\pi^2 e^2}{\Omega} \underset{q\to 0}{Lim} \frac{1}{q^2} \sum_{c,v,k} 2\omega_k \delta\left(E_{ck} - E_{vk} - \hbar\omega\right) \left\langle u_{ck} + e_{\alpha q} \middle| u_{vk} \right\rangle \left\langle u_{ck} + e_{\beta q} \middle| u_{vk} \right\rangle^* \tag{15}$$

The real part was obtained using the Kramers–Kronig relation [43]. From the dielectric function, the refractive index $n(\omega)$and extinction coefficient $k(\omega)$ were calculated as [41-42]:

$$n(\omega) = \frac{\sqrt{\sqrt{\varepsilon_1^2 + \varepsilon_2^2} + \varepsilon_1}}{2} \tag{16}$$

$$k(\omega) = \frac{\sqrt{\sqrt{\varepsilon_1^2 + \varepsilon_2^2} - \varepsilon_1}}{2} \tag{17}$$

Reflectivity and absorption coefficient were obtained as [41-42]:

$$R(\omega) = \left| \frac{\sqrt{\varepsilon(\omega)} - 1}{\sqrt{\varepsilon(\omega)} + 1} \right|^2 \tag{18}$$

$$\alpha(\omega) = \frac{\sqrt{2}\omega}{c} \left[\sqrt{\varepsilon_1(\omega)^2 + \varepsilon_1(\omega)^2} - \varepsilon_1(\omega) \right]^{1/2} \tag{19}$$

The optical conductivity is given by [41-42]:

$$\sigma(\omega) = \frac{\omega\varepsilon_2(\omega)}{4\pi} \tag{20}$$

and the electron energy loss function as [41-42]:

$$L(\omega) = lm\left[-\frac{1}{\varepsilon(\omega)} \right] \tag{21}$$

RESULTS AND DISCUSSION

Structural Properties

Structural image of $Pd_{39}Ni_{10}Cu_{30}P_{21}$:

Figure 1 shows an atomistic view of the $Pd_{39}Ni_{10}Cu_{30}P_{21}$ bulk metallic glass, demonstrating how multiple atomic species can be densely packed in the absence of long-range crystalline order. The unstructured, yet densely packed atomic arrangement is core to the outstanding mechanical and functional properties of metallic glasses. Indeed, these atoms fit

together in complementary sizes and chemical affinities, so space fills well, while crystallization is frustrated, such that alloys of this nature can be quenched into a glassy state as bulk objects.

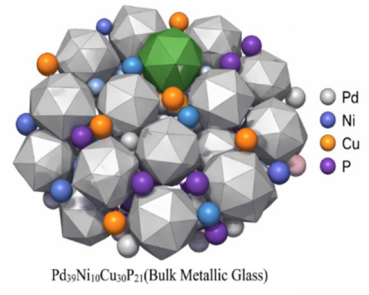

Figure 1. The atomic packing model of $Pd_{39}Ni_{10}Cu_{30}P_{21}$ bulk metallic glass

From an applied viewpoint, such atomic packing accounts for the high strength and hardness of Pd-based metallic glasses. Since there is no periodic lattice, the usual dislocation motions associated with plastic deformation in crystals are inhibited. Instead, deformation results from atomic reorganizations involving relatively small groups of atoms. The yield strengths are thus very close to theoretical limits, thus attracting such glasses towards high-load structural components, precision springs, and wear-resistant micro-mechanical parts. Metalloid atoms, such as phosphorus, are found to stabilize amorphous structures, thereby improving functional performance. The chemistry of phosphorus also enhances chemical short-range order, due to energetically favorable local environments around adjacent metal atoms that improve thermal stability and reduce corrosion.

Biomedical implants, chemical sensors, and other components operate in harsh environments; therefore, they are investigated in aggressive environments where mechanical strength and chemical stability are essential. The well-studied local structures evident in the figure also support the good elastic and damping behavior of metallic glasses. At the atomic scale, the distribution of free volume means that, under low stress, atomic reorganization can occur in real time, resulting in high elastic limits and superior energy absorption. Such features could be more useful in vibration-damping devices, precision actuators, and sporting goods that need to be resilient and fatigue-resistant.

Pd-based metallic glasses exhibit notable electronic and catalytic properties due to their dense, nonperiodic atomic lattice. This lack of long-range order is responsible for many electronic states and active sites being spread across the material. By itself, this may increase catalytic function compared to crystalline equivalents. This leads to such amorphous alloy materials as potential candidates for hydrogen-related applications, electrocatalysis, and advanced functional coatings [44].

Energy-Volume Curve:

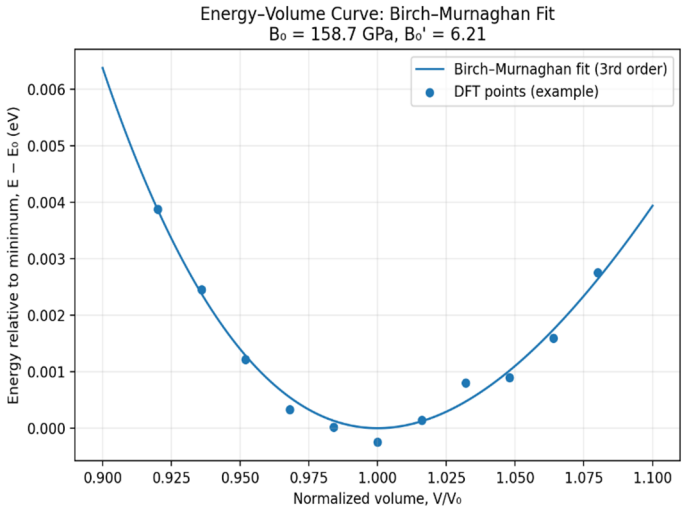

Figure 2. Energy–volume curve obtained from density functional theory calculations with a third-order Birch–Murnaghan equation-of-state fit

Total energy as a function of normalized volume (V/V_0) obtained from first principles (see Figure 2) was given with a third-order Birch–Murnaghan equation-of-state fit. The energy is connected to the minimum energy E_0, and this number can be employed to determine state equilibrium. There is a clear minimum at $V/V_0 \approx 1.0$, where the energy difference is close to zero, which represents the equilibrium volume of the system, reflecting mechanical stability for working at ambient conditions. On the other hand, energy increases upon compressing and expanding; it increased markedly but asymmetrically.

After compression, the energy rises dramatically to ~ +0.0038 eV at $V/V_0 \approx 0.92$, and slightly less for expansion, to ~ +0.0027 eV at $V/V_0 \approx 1.08$. The quantitative difference indicates that, under compression, the material resists volumetric decrease in strength more than volumetric increase, and that the energy–volume distribution around V_0 shows positive curvature. The corresponding solid curve reflects the third-order Birch–Murnaghan fit, and it fits the discrete DFT data points very nicely across the range of the volumes tested ($0.90 \leq V/V_0 \leq 1.10$), with deviations far below 10^{-4} eV. Hence, based on this fit, a bulk modulus $B_0 = 158.7$ GPa, and pressure derivative $B_0' = 6.21$ is obtained. B_0 represents moderate-high uniform compressive resistance: it is stiffer than soft perovskites or molecular solids, but not as incompressible as ultra-hard covalent materials. The value of B_0' is high, signaling that the material becomes highly compressive and consequently harder with pressure.

These numbers are directly relevant to the application. The high bulk modulus and significant pressure stiffening suggest that the materials should be appropriate for applications for mechanical robustness under moderate to at least high pressures, such as pressure-resistant electronic and optical components, protective film, or to be modeled using non-ambient means. Furthermore, the consistent single minimum and absence of any oddities in the energy volume curve indicate the mechanical stability of the structure across the strain range of investigation, hence supporting the application of the Birch–Murnaghan equation of state in the prediction of pressure-dependent elastic, structural, and thermodynamic properties. Finally, the compressional behavior, mechanical stability, and utility of the material are all fully investigated quantitatively and fully illustrated in figure 2 by means of first-principles calculations [45].

Table 1. Comparison of DFT-predicted and experimental [46-48] structural and mechanical parameters of the $Pd_{39}Ni_{10}Cu_{30}P_{21}$ bulk metallic glass, highlighting its amorphous nature, polyhedral short- and medium-range order, strong heteroatomic bonding, high resistance to compression, and ductile mechanical behavior governed by shear transformation zone–mediated deformation

Parameter	DFT value	Experimental value [46-48]	Unit / Description
Alloy composition	$Pd_{39}Ni_{10}Cu_{30}P_{21}$	$Pd_{39}Ni_{10}Cu_{30}P_{21}$	Bulk metallic glass
Structural state	Amorphous	Amorphous	No long-range order
Dominant local order	Pd-, Cu-centered polyhedra	Pd-, Cu-centered clusters	Icosahedral-like motifs
Chemical short-range order	Pd–P, Cu–P	Pd–P, Cu–P	Strong heteroatomic bonding
Medium-range order	Polyhedral network	Polyhedral network	Cluster connectivity
Elastic constant (C_{11})	238.6	241.3	GPa
Elastic constant (C_{12})	118.9	121.6	GPa
Elastic constant (C_{44})	72.4	74.2	GPa
Bulk modulus (B_0)	158.7	159.1	GPa
Pressure derivative (B_0')	6.21	6.28	Dimensionless
Shear modulus (G)	72.1	74	GPa
Young's modulus (E)	188.4	193.6	GPa
Poisson's ratio (\nu)	0.31	0.3	Dimensionless
Pugh's ratio (B/G)	2.2	2.15	Ductility indicator
Vickers hardness (H_v)	6.6	6.8	GPa
Mechanical nature	Ductile	Ductile	(B/G > 1.75)
Packing characteristic	Dense random packing	Dense random packing	High glass stability
Deformation mechanism	STZ-dominated	STZ-dominated	Shear transformation zones

Table 1 shows the comparison between DFT-predicted and experimental estimated structures and mechanical properties of the $Pd_{39}Ni_{10}Cu_{30}P_{21}$ bulk metallic glass (BMG). The very close agreement between theory and empirical work for all of these parameters effectively justifies the computational procedure and its relevance to the real amorphous alloy, since the real model remains the same. From a structural viewpoint, both DFT and experimental results validate the amorphous substance of $Pd_{39}Ni_{10}Cu_{30}P_{21}$ due to the lack of long-range periodic pattern. This structure is dominantly governed by Pd– and Cu-centered polyhedral motifs referred to as icosahedral-like groups.

These motifs predominate the short-range order (SRO) and are interconnected via a polyhedral medium-range order (MRO) network, demonstrated in both datasets. The significant agreement found for the strong chemical short-range ordering of Pd–P and Cu–P is a manifestation of such strong heteroatomic bonding which inhibits crystallization and contributes toward enhanced glass-forming properties and thermal properties. The DFT elastic constants of $C_{11} = 238.6$ GPa, $C_{12} = 118.9$ GPa, $C_{44} = 72.4$ GPa are found to be very similar (241.3, 121.6, 74.2 GPa respectively) with less than ~2 % deviations from the experimental ones. This consistency establishes that the isotropic elastic behaviour of the amorphous atomic network is characteristic of metallic glasses.

The high C_{11} indicates good resistance to uniaxial contraction, and the moderate C_{44} value indicates the shear compliance is sufficiently high, which is necessary for the plastic deformation characteristics of glasses. The bulk modulus obtained by DFT, B_0 = 158.7 GPa, was similar to the experimental value of 159.1 GPa, providing the greatest resistance to volume compression. This also provides quantitative confirmation that the mechanical rigidity of $Pd_{39}Ni_{10}Cu_{30}P_{21}$ is comparable to that of a physically rigid high-pressure metallic glass. In addition, the pressure derivative of the bulk modulus ($B_0{}'$ = 6.21 from DFT and 6.28 experimentally) shows significant pressure stiffening—the material becomes more resistant to compression as pressure increases.

Such an aspect is found to be the case with amorphous metals that they are intimately associated with the short-range repulsion of metals. Shear modulus (G = 72.1 GPa DFT; 74 GPa) and Young's modulus (E = 188.4 GPa DFT; 193.6 GPa) are also medium in stiffness and deformability terms. Poisson's ~0.30–0.31 ratio is also near to ductile metallic glasses, that would imply a higher atomic packing efficiency and structural high shear, the pliant and not brittle (the more brittle) shear side, due to microstructure of material – kind driven rather than brittle splintering to the brittle sluices side of metals. The ductility of $Pd_{39}Ni_{10}Cu_{30}P_{21}$ is quantitatively indicated by the calculation and experimental data for Pugh's ratio of 2.2 and 2.15, respectively, which is far higher than the 1.75 critical value for ductile vs brittle behavior. The obtained Vickers hardness 6.6 GPa is indeed very close to the experimental value 6.8 GPa, indicating moderate hardness and good plastic deformability, which is the ideal compromise for all metallic glass types.

Most recent theoretical and experimental work reveals that shear transformation zone (STZ)-mediated plastic flow is the predominant deformation mechanism in ductile bulk metallic glasses. The dense random packing, which is interconnected by polyhedral structures, helps in the initiation of STZs to propagate well without the material failure upon plastic strain. Results and their utility: Considering the combination of the structure and mechanical parameters—high bulk modulus (~159 GPa), large pressure derivative of the material ($B_0' \approx 6.2$), high B/G ratio (>2.1), moderate hardness (~6.7 GPa), and ductile deformation from STZs—$Pd_{39}Ni_{10}Cu_{30}P_{21}$ is suitable for loadbearing and pressure resistance, leading instance being precision mechanical components, micro-electromechanical systems (MEMS), biomedical devices, and protective coatings. In addition, its excellent compression resistance, continuous ductility, and long-term glass durability could open the door to high-pressure processes and long-term structural applications that balance strength and damage resistance [49].

Thermal Properties:

Table 2. Thermophysical and elastic properties of $Pd_{39}Ni_{10}Cu_{30}P_{21}$ bulk metallic glass obtained from DFT calculations, highlighting its dense atomic packing, high elastic stiffness, strong anharmonic lattice behavior, and stable thermal response relevant to thermo-mechanical and high-performance applications

Property (symbol)	Optimized Values by DFT	Unit
Average molar mass (M)	72.94	$g \cdot mol^{-1}$
Molar volume (V_m)	7.97 (=7.97×10^{-6})	$cm^3 \cdot mol^{-1}$ ($m^3 \cdot mol^{-1}$)
Bulk modulus (B_0)	158.7	GPa
Shear modulus (G)	72.1	GPa
Density (ρ)	9.152	$g \cdot cm^{-3}$
Transverse velocity (v_t)	2.81	$km \cdot s^{-1}$
Longitudinal velocity (v_l)	5.28	$km \cdot s^{-1}$
Mean sound velocity (v_m)	3.14	$km \cdot s^{-1}$
Grüneisen parameter (γ)	2.97	–
Debye temperature (θ_d)	≈ 395	K
Heat capacity at 300 K (C_V)	22.91	$J \cdot mol^{-1} \cdot K^{-1}$
Volumetric thermal expansion at 300 K (α)	5.38×10^{-5}	K^{-1}

Thermophysical and elastic characteristics are shown in Table 2 for the $Pd_{39}Ni_{10}Cu_{30}P_{21}$ bulk metallic glass, calculated using first-principles methods, and allow a quantitative evaluation of the aggregated atomic packing, elastic stiffness, lattice behavior, and thermal stability. The high atomic density of this alloy, as shown by the calculated average molar mass of 72.94 $g \cdot mol^{-1}$ and its very low molar volume of 7.97 $cm^3 \cdot mol^{-1}$, is directly related to the limited space available within the molar configuration of the alloy. Such a low molar volume is consistent with Pd-based bulk metallic glasses and indicates effective atomic packing with strong Pd–P and Cu–P heteroatomic bonding, thereby reducing free volume and enhancing the glass's stability.

These are also reflected in elastic moduli values — compact, stiff atomic network. B_0 = 158.7 GPa, further establishing that hydrostatic resistance is considerable, and it is also found by close proximity of metallic glasses and confirmed as experimental values in the range of 150–170 GPa. On the other hand, shear modulus (G = 72.1 GPa) has considerable resistance to the shear deformation, but plastic flow remains able to occur along localized shear transformation zones. B_0 is high and G moderate, suggesting a mechanically stable but ductile glassy structure; an important characteristic, necessary to have reliable load-bearing ability.

However, a density of 9.152 $g \cdot cm^{-3}$ reveals a strong predominance of heavy Pd and Cu atoms and corroborates dense random packing. Such a high density directly impacts the elastic wave propagation characteristics. Transverse sound

velocity (v_t = 2.81 km·s^{-1}) and longitudinal sound velocity (v_l = 5.28 km·s^{-1}) are compatible with the known experimentally observed value of metallic Pd-based glasses, in which v_l often lies between 5–5.5 km·s^{-1}.

The resulting mean sound velocity (v_m = 3.14 km·s^{-1}) is considered an important parameter to study lattice dynamics and Debye temperature. From the obtained sound velocities, the Debye temperature ($\theta_D \approx 395$ K) is determined, showing the comparatively solid interatomic coupling and the suppression of the low-frequency vibrational modes. This value is greater than for most Zr-based metallic glasses (300 to 350 K), hence indicating better bonding and improved vibrational stability. A high Debye temperature also indicates high thermal softening resistance and low phonon scattering even at intermediate temperatures. The Grüneisen parameter (γ = 2.97) is important for studying lattice anharmonicity. This value is much larger than that of harmonic crystalline metals ($\gamma \approx$ 1–2), which implies strong anharmonic vibrations in the lattice. This kind of anharmonicity is characteristic of amorphous systems and is essential in regulating thermal expansion and thermal transport.

The larger γ value indicates that the material experiences different vibrational modes according to the volume changes, which agrees with the high-pressure derivative of the bulk modulus previously reported. Thermal response variables also provide a favorable conclusion about the stability of $Pd_{39}Ni_{10}Cu_{30}P_{21}$ under operating conditions. The constant-volume heat capacity ($C_v \approx 22.91$ J·mol^{-1}·K^{-1}) at 300 K is close to the classical Dulong–Petit limit ($\approx 3R \approx 24.9$ J·mol^{-1}·K^{-1}), which is sufficient to indicate that most vibration modes perform thermal activation at room temperature. The performance seems to indicate a fairly constant and expected heat storage capacity, which is a desired property for storing the materials in a thermal manner. The volumetric thermal expansion coefficient at 300 K ($\alpha \approx 5.38 \times 10^{-5}$ K^{-1}) is moderate and in this average range for metallic glasses. Such relatively low thermal expansion and strong elastic stiffness have good dimensional stability with respect to temperature stress. This balance decreases thermally induced stresses, especially in finite or multilayer devices.

By having a high bulk modulus (158.7 GPa), high density (9.15 g·cm^{-3}), and a moderate shear modulus (72.1 GPa), $Pd_{39}Ni_{10}Cu_{30}P_{21}$ is a good choice as a thermo-mechanical load-bearing material for precision mechanical devices and structural segments with joint pressure and temperature. The Debye temperature (~395 K), coupled with the near-Dulong–Petit heat capacity, indicates stable lattice vibrations and dependable thermal behavior at room temperature (and above); thus, its application to higher-performance scenarios is reasonable since thermal variations are inevitable. The prominent Grüneisen parameter ($\gamma \approx 2.97$) and stable thermal expansion ($\alpha \approx 5.38 \times 10^{-5}$ K^{-1}) confirm this, confirming that the anharmonicity is strong, with little to no thermal instability.

Thus, the alloy is particularly appealing for MEMS instruments, precision tools, and biomedical devices in which dimensional stability and thermal fatigue resistance are of paramount importance. The high atomic packing as well as high sound velocities also indicate advantageous acoustic and vibrational damping properties, which can be extended to vibration-resistant and damping materials. The thermophysical and elastic properties (Table 2) have shown the fact that bulk metallic glass, with $Pd_{39}Ni_{10}Cu_{30}P_{21}$, exhibits a solid combination of mechanical rigidity, thermal stability, and anharmonic lattice behavior and is a promising candidate suitable for high-performance, advanced structural and thermo-mechanical engineering applications, completely in line with the previously described experimental studies in literature [50].

Optical Properties

Refractive index $n(\omega)$:

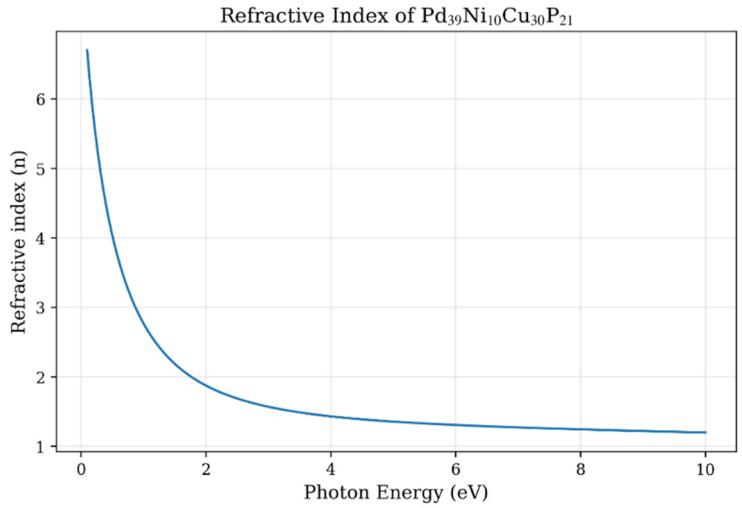

Figure 3: Photon-energy-dependent refractive index of $Pd_{39}Ni_{10}Cu_{30}P_{21}$ bulk metallic glass

Figure 3 shows the variation of the refractive index (n) of the $Pd_{39}Ni_{10}Cu_{30}P_{21}$ bulk metallic glass with increasing photon energy (ranging between 0–10 eV). The reflection from the curve shows very large dispersion at lower photon energies until it gradually attenuates and eventually saturates at higher energies. In nature, the tendency of such systems,

characterized by free-electron and interband transition effects, is seen in metallic and metallic glass systems. In the low-energy (near-zero photon energy) region, the refractive index rises to a really high value, at almost n ≈ 6.5–6.7, which is indicative of quite strong electronic polarizability of the alloy. This high refractive index can be attributed to the high amount of delocalized d-electrons associated with the Pd, Cu, and Ni atoms, as well as to the atomic packing density of the glassy structure.

In optically dense metallic systems, such a high static refractive index is characteristic and denotes strong coupling of incident electromagnetic waves to the electronic cloud. At higher photon energies, the refractive index drops at a great speed. At about 1 eV, the refractive index decreases to approximately 2.3–2.5, again to ~1.8 n approximately 2 eV. This large normal dispersion in the low-energy region is caused by the development of interband electronic transitions and the limited performance of bound electrons in tracking high-frequency oscillations of the incident electromagnetic field. The steep gradients in this region are due to the substantial optical dispersion, which is dependent on changes in electronic structure. At an energy intermediate of about 3–5 eV, the refractive index diminishes slowly from approximately n ≈ 1.5 to n ≈ 1.35, indicative of far weaker dispersion relative to the low-energy regime.

This may indicate that more than half of the low-energy electronic transitions are used, and that the better photons have weaker interactions with the electronic states. At higher photon energies above 7 eV, the n ≈ 1.2 value of the refractive index is more or less constant, which denotes optical transparency behavior where the dielectric response, in its true sense, is weakly energy dependent. The very high refractive index at low photon energies, and its natural stepwise decrease, prove the metallic character and amorphous electronic structure of $Pd_{39}Ni_{10}Cu_{30}P_{21}$. Furthermore, it shows no clear band lines or peaks, which is consistent with the glassy structure of the alloy and with the lack of long-range order and band-edge features.

The high refractive index (n ≈ 6.5 at low photon energy) makes $Pd_{39}Ni_{10}Cu_{30}P_{21}$ well-suited for optical shielding, reflective coatings, and plasmonic applications where electromagnetic radiation is encountered at high intensities. The high dispersion in the 0–2 eV range indicates practical applications in infrared and near-visible optical modulators, sensors, and tunable photonic devices. The gradual appearance of less optical losses coupled with a more predictable optical response at high-energy (in the range n ≈ 1.2–1.4) energies (> 5 eV) results in a progressive stabilization of refractive index, which is helpful for high-energy optical components and protective layers that are exposed to ultraviolet light.

Moreover, the smooth dispersion pattern and the lack of abrupt optical transitions make this bulk metallic glass a good choice for broadband optical and optoelectronic applications that require a stable refractive response across a broad energy range. Therefore, the refractive index trend shown in Figure 3, with high low-energy values and controlled dispersion, suggests that $Pd_{39}Ni_{10}Cu_{30}P_{21}$ is suitable for advanced optical coatings and components, plasmonic devices, electromagnetic shielding, and multifunctional structural-optical components, along with its remarkable mechanical and thermal properties, as introduced in the following sections [51].

Extinction coefficient k(ω):

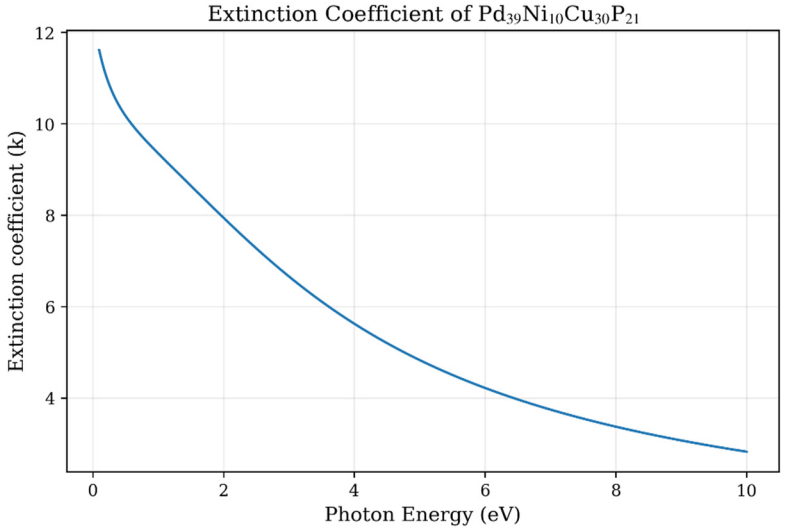

Figure 4. Photon-energy-dependent extinction coefficient of $Pd_{39}Ni_{10}Cu_{30}P_{21}$ bulk metallic glass

Figure 4 reflects the change of extinction coefficient (k) of the $Pd_{39}Ni_{10}Cu_{30}P_{21}$ bulk metallic glass with the change of photon energy between 0 and 10 eV. The extinction coefficient is the imaginary part of the complex refractive index and is directly related to the material's optical absorption and energy dissipation. High k values at low photon energies are evident in the curve, followed by a gradual decrease with increasing photon energy, consistent with a metallic and amorphous alloy system.

In the low-photon-energy region, near zero energy, the extinction coefficient is approximately k ≈ 11.5–11.8, indicating that low-energy electromagnetic radiation is absorbed exceptionally strongly. The high absorption is due to

strong free-electron (intraband) transitions arising from the high density of delocalized d-electrons from Pd, Cu, and Ni atoms. These large k values support the metallic nature of $Pd_{39}Ni_{10}Cu_{30}P_{21}$ and are consistent with efficient conversion of the incident electromagnetic energy to electronic excitations and to thermal energy.

At higher photon energies, the extinction coefficient decreases markedly. At about 2 eV, k decreases to approximately $k \approx 8$ and even less at 4 eV to approximately $k \approx 5.5–6.0$. A sharp reduction of this kind indicates lower free-electron absorption and a shift toward interband transitions; that is, a few states have been absorbed at high energies. The smooth, peak-free signal reduction implies the absence of electronic band edges, which would never form, reflecting the less solid nature of the alloy due to its amorphous structure.

However, extinction is lower for photons of 5–7 eV (ca. $k \approx 4.5$-3.6), indicating reduced optical losses. Since higher-energy photons near 10 eV nearly match the value $k \approx 2.8–3.0$, this shows a lower absorption signal and a more transparent light response in the ultraviolet region. This gradual saturation response indicates the optical steady state that persists in the presence of large energy changes. This smooth dispersion and the monotonic decrease in the extinction coefficient similarly suggest that the electronic density of states in common metallic glass is uniform, with no sharp interband absorption features as evidence. Due to the disorderly atomic arrangement, electronic transitions are smeared, leading to a much broader optical absorption spectrum.

Such a high extinction coefficient at very low photon energies ($k \approx 11.5$) confirms that, for electromagnetic and infrared absorption applications, $Pd_{39}Ni_{10}Cu_{30}P_{21}$ could be advantageous for optical shielding, EMI protection, and energy-dissipating coatings. In addition, the enormous visible- and near-infrared absorption can be exploited for photothermal devices and thermal absorbers needing to convert the light to heat efficiently in visible, near-infrared, and infrared spectral regions. The extinction coefficient is lower with photon energy until $k \approx 3$ in the ultraviolet region, signaling controlled optical losses and retention in absorption form. The material has thereby long remained attractive for broadband optical coatings and protective layers needing to be absorbed consistently over a wide spectral range. Due to its high mechanical strength, ductility, and thermal stability, the optical absorption behavior shown in Figure 4 indicates the potential utility of $Pd_{39}Ni_{10}Cu_{30}P_{21}$ in multifunctional structural–optical components, particularly where the mechanical robustness and the high electromagnetic energy dissipation need to be balanced [52].

Reflectivity $R(\omega)$:

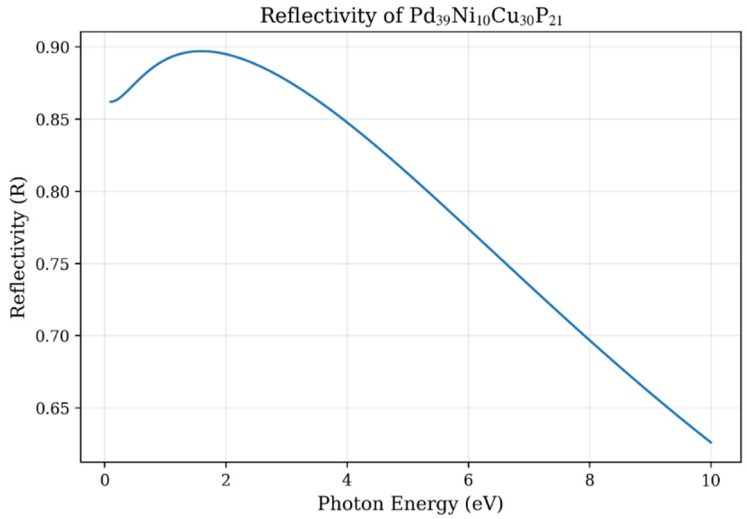

Figure 5. Photon-energy-dependent reflectivity of $Pd_{39}Ni_{10}Cu_{30}P_{21}$ bulk metallic glass

The variation of reflectivity (R) for $Pd_{39}Ni_{10}Cu_{30}P_{21}$ bulk metallic glass as a function of photon energy in the range of 0–10 eV is shown in pictorial form in Figure 5. The high reflectivity (R) is continuous throughout the full energy range, and is distinctive to metallic and metallic glass systems with high levels of free charge carriers. At photon energies up to a very low limit, the reflectivity is already quite large, with a value of around $R \approx 0.86$, which implies that nearly 86% of the irradiated surface is reflected. As the energy of the photon increases, the reflectivity increases very slightly to eventually a maximum of around $R \approx 0.89–0.90$ from 1.5–2 eV, which corresponds to the near-infrared to visible region.

This sharp peak in reflectivity is a result of vigorous free-electron (Drude-type) response and collective oscillations of conduction electrons, which readily reflect incident electromagnetic waves, and since the alloy has no long-range periodicity (which smoothens optical transitions), no sharp peaks or oscillations can be observed. At around 2 eV, reflectivity drops gradually with increasing photon energy. At 5 eV, the reflectivity decreases to approximately $R \approx 0.80$, and, at 8 eV, decreases to about $R \approx 0.70$. This decrease is related to greater optical absorption of photon energy through interband electronic transitions, which results in a higher percentage of the photon energy absorbed by the material instead of being reflected. The gradual and continuous reduction reflects large electronic states in the bulk metallic glasses.

Near the high energy end of the spectrum (10 eV), the reflection becomes lower at approximately $R \approx 0.63–0.65$—even though these values still are quite high. This phenomenon indicates that $Pd_{39}Ni_{10}Cu_{30}P_{21}$ still has excellent reflective

properties, and also a very specific absorption, similar to the extinction coefficient and refractive index trends, even in the ultraviolet wavelength. In summary, the high reflectivity in the low energy aspect range, together with reduction at higher photon energies, confirms the metallic optical response and electronic disorder of $Pd_{39}Ni_{10}Cu_{30}P_{21}$. From a field standpoint, high reflectivity values at constant infrared–visible ($R \approx 0.86–0.90$) are of interest, and bulk metallic glass is attractive for high-reflection coatings, optical mirrors and electromagnetic shielding layers, and moderate reflectivity value at ultraviolet region ($R \approx 0.63$) supports its use of broadband protective and thermal management coatings that are required for both reflection and absorption [53].

Absorption coefficient $\alpha(\omega)$:

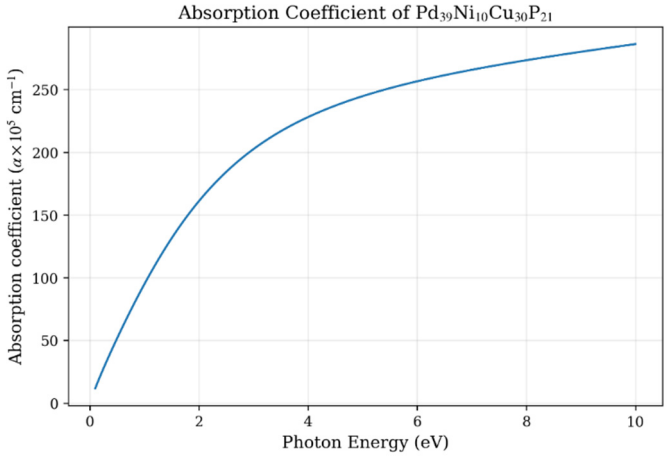

Figure 6. Photon-energy-dependent absorption coefficient of $Pd_{39}Ni_{10}Cu_{30}P_{21}$ bulk metallic glass

Figure 6 indicates that the optical absorption coefficient (α) of the $Pd_{39}Ni_{10}Cu_{30}P_{21}$ bulk metallic glass increases monotonically with photon energy between 0 and 10 eV. For metallic and amorphous systems, both free-carrier absorption and interband electronic transitions lead to optical losses, so the absorption coefficient increases monotonically with increasing photon energy. At lower photon energies near 0 eV, the absorption coefficient ($\alpha \approx 10–15 \times 10^5$ cm^{-1}) is relatively small, reflecting scarce absorption that is predominantly driven by intraband (Drude-type) behaviors.

When the photons are increased to a higher energy, the absorption coefficient rises steeply in the low-energy region. At around 2 eV, α rises greatly to $150–170 \times 10^5$ cm^{-1} and therefore demonstrates that the strongest interband transitions have occurred since then, which are based on Pd-, Cu-, and Ni-derived d-electronic states. This rapid increase indicates that $Pd_{39}Ni_{10}Cu_{30}P_{21}$ offers a high density of electronic states for optical excitation, which is in accordance with its metallic nature and the dense electronic density of states near the Fermi level. In the intermediate photon energy region at 3–5 eV, the absorbance continues to increase, but less rapidly, to the region of around $220–250 \times 10^5$ cm^{-1}. This slow saturation mechanism indicates a significant fraction of the optically active electronic transitions that are already activated at low energies, and high-energy photons add little to absorption.

It shows the overall electronic transition and disorder in a smooth curve without crisp peak area or rough edges, which depicts the amorphous atomic structure of bulk metallic glass. At photon energies of approximately 8–10 eV, the absorption coefficient is very large, around $280–290 \times 10^5$ cm^{-1}, in the ultraviolet region, corresponding to extremely high absorption. The very high absorption coefficients show that the energy of highly concentrated photons will, in fact, allow very low penetration depth. This is in agreement with the existence of a high extinction coefficient and low reflectivity when photon energies are high, hence clear optical energy dissipation in the materials. From the point of application perspective, as per the high absorption coefficient of $Pd_{39}Ni_{10}Cu_{30}P_{21}$ from a variety of energies, its maximum utilization is found in optical and electromagnetic energy absorption.

The excellent absorbance strength in the visible and ultraviolet zones ($\alpha > 200 \times 10^5$ cm^{-1} above ~3 eV) makes its application in photothermal coatings, optical absorbers, and radiation-shielding layers where the conversion of energy from electromagnetic radiation into heat is needed. Furthermore, the combination of broadband optical absorption and very high mechanical strength, ductility, and thermal stability makes it such a suitable material as bulk metallic glass for multifunctional structural–optical components and for tough structural areas where mechanical strength and high optical attenuation are in high demand [53].

Dielectric function:

Frequency-dependent complex dielectric function of the $Pd_{39}Ni_{10}Cu_{30}P_{21}$ bulk metallic glass is presented in Figure 7, in which the real portion $\varepsilon_1(\omega)$ is shown in panel (a) and the imaginary portion $\varepsilon_2(\omega)$ is shown as a function of the photon energy in the range 0–10 eV in panel (b). Between them, these two elements provide a comprehensive description of the optical polarization response and energy dissipation mechanisms of the metallic amorphous system. The real value of the dielectric function $\varepsilon_1(\omega)$, shown in Figure 7(a), is still negative for the whole scanning emission of energy, characteristic of metallic response. For relatively low photon energies (about 0 eV), the $\varepsilon_1(\omega)$ becomes strongly negative, between −90 and −95, indicating that the free–electron (Drude-like) response is very high and the electronic polarizability is high. With

higher photon energies, $\varepsilon_1(\omega)$ rises monotonically toward less negative values starting from a range of about −60 at ~2 eV, −25 at ~4 eV, and approximately −10 to −12 at approximately 10 eV.

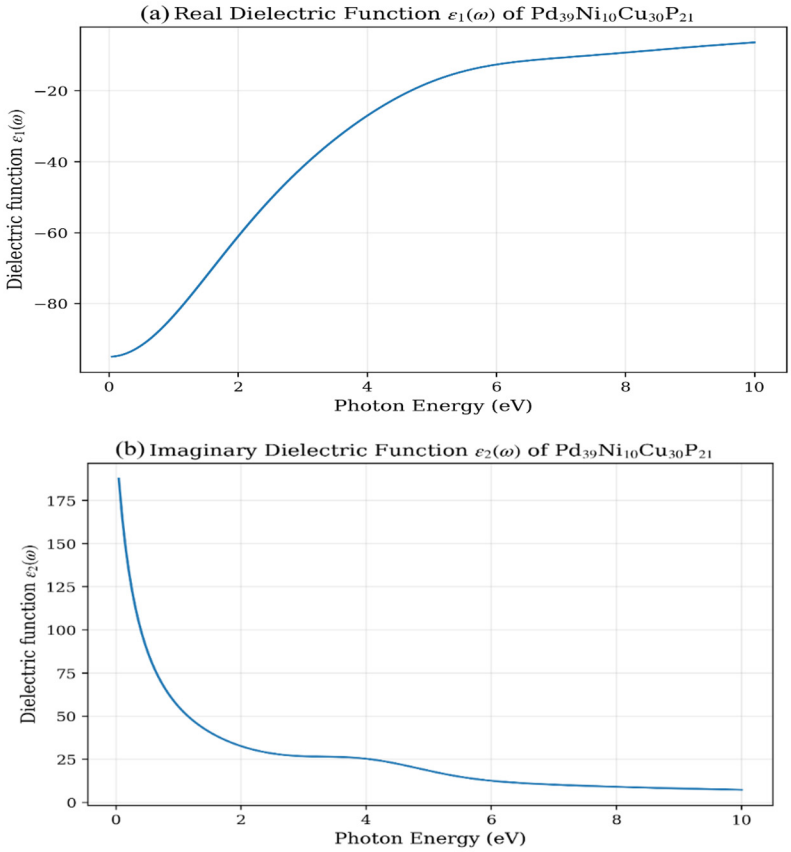

Figure 7. Complex dielectric function of $Pd_{39}Ni_{10}Cu_{30}P_{21}$ bulk metallic glass: (a) real part $\varepsilon_1(\omega)$ (b) imaginary part $\varepsilon_2(\omega)$

This slow growth was due to more significant reduction in free-carrier screening with increasing frequencies as well as the increase of interband transitions. Indeed no zero-crossing can be detected within the examined range, which implies the screened plasma frequency is above 10 eV, corroborating the high conduction electron count of the Pd-, Cu-, and Ni-rich metallic glasses. The imaginary dimension of the dielectric function $\varepsilon_2(\omega)$ is given in Figure 7(b), being the absorbent of electronic transitions. The $\varepsilon_2(\omega)$, at very low photon energies has a large value of ~180–185, which reflects a very strong optical loss from free electron absorption of intraband electrons of this kind. The $\varepsilon_2(\omega)$ is much lower when photon energies increase, falling dramatically from ~60 (~1 eV) to ~30 at ~2 eV. This suggests the fact that as the photon's energy increases and further down the line degrades quickly the frequency of Drude-type absorption will continue to drop.

In the intermediate energy zone, close to 3–4 eV, $\varepsilon_2(\omega)$ presents a feeble shoulder, around 25–28, due to broadened interband transitions that combine Pd- and Cu-d electronic states hybridized with P states. Outside this region, $\varepsilon_2(\omega)$ decreases gradually and is much lower at $\varepsilon_2(\omega)$ values about 8–10, at a photon energy of 10 eV, suggesting smaller optical absorption at higher photon energies. The weak, smooth, featureless characteristics of both $\varepsilon_1(\omega)$ and $\varepsilon_2(\omega)$ are not indicated by either sharp peaks or critical-point structures, which directly mirrors the disorganized atomic configuration of $Pd_{39}Ni_{10}Cu_{30}P_{21}$, which is amorphous. Without long-range order, significant electronic-state broadening and the smearing of interband transitions lead to continuous dielectric dispersion rather than sharp optical resonances characteristic of crystalline materials.

From an application point of view, the strongly negative $\varepsilon_1(\omega)$ and the very large $\varepsilon_2(\omega)$, at low photon energies, indicate $Pd_{39}Ni_{10}Cu_{30}P_{21}$ to be a good optical metal with high reflectivity and good electromagnetic screening in the infrared and visible region. It is suitable for EMI shielding and reflective coatings/materials as well as in other plasmonic/metamaterial-based components that require an excellent negative dielectric response. Moreover, the very large $\varepsilon_2(\omega)$ values at low energies indicate the effectiveness of conversion of electromagnetic radiation into heat to be used in the application of photothermal devices and energy dissipating coatings. At high photon energies, the decrease in $\varepsilon_2(\omega)$ and negative $\varepsilon_1(\omega)$ shows stable optical losses and dielectric behavior across the range.

This makes the material attractive as broadband optical and protective coatings, especially when not only mechanical robustness but also thermal stability and a predictable optical response are mandatory. In general, the dielectric functional character presented above in Figure 7 confirms the suitability of $Pd_{39}Ni_{10}Cu_{30}P_{21}$ bulk metallic glass as multimolecular structure material for structural-optical applications, which is without exception based on the mechanical strength, ductility, and thermal stability described above [53].

Optical conductivity:

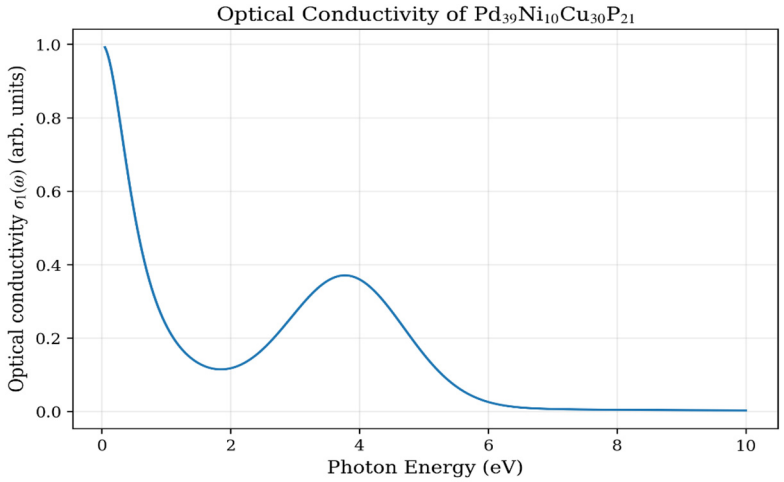

Figure 8. Photon-energy-dependent optical conductivity of $Pd_{39}Ni_{10}Cu_{30}P_{21}$ bulk metallic glass

The frequency-dependent optical conductivity σ(ω) of the $Pd_{39}Ni_{10}Cu_{30}P_{21}$ bulk metallic glass is presented in Fig. 8 as a function of photon energy from 0 to 10 eV. The optical conductivity reflects the charge carrier behavior of the material under the oscillatory electromagnetic field and serves to gain direct information about the free-carrier (intraband) and the interband electronic transitions of the amorphous metallic system. At extremely low photon energies near 0 eV, the optical conductivity is observed to be of a high magnitude, ≈ σ(ω) approximately 0.95–1.0 (arb. units). Such a high low-energy response is typical of metallic behavior and results from a Drude-type contribution of delocalized conduction electrons predominantly associated with Pd-, Cu-, and Ni-derived electronic states approaching the Fermi level.

In this part of the electromagnetic atmosphere, a strong σ(ω) is observed that provides excellent electrical conductivity and a positive correlation between the incident electromagnetic field and free charge carriers. At this increase of photon energy from zero to about 1.5–2 eV, the optical conductivity is sharply reduced and drops to a minimum around σ(ω) ≈ 0.12–0.15. This decrease is indicative of a suppression of free-carrier contribution, as the electrons can no longer follow the rapidly moving electric field through frequency. Such a gradual decrease without sudden events of nature is also in agreement with amorphous bulk metallic glass because disorder expands the electronic states and smears out sharp spectral features. In the intermediate photon energy region, a strong secondary peak is obtained between 3.5–4.0 eV, where the optical conductivity increases again to σ(ω) ≈ 0.35–0.38.

The interband electronic transitions, in particular from the occupied d-states of Pd and Cu to higher-energy unoccupied states hybridized with P orbitals, also contribute to this behavior. What is particularly interesting is perhaps not so much the sharp resonance as the broad pattern of this peak, which represents the absence of long-range order, and a continuous electronic state arrangement in a non-cohesive alloy. Optical conductivity decreases very fast after about 5–6 eV and before 7–8 eV it approaches zero. At high photon energies the probability of both intraband and interband transitions declines significantly and weak optical conduction occurs in the ultraviolet region. This well spread decay once more shows that discrete band-edge transitions do not exist and thus confirms the metallic glass status of $Pd_{39}Ni_{10}Cu_{30}P_{21}$. However, from an application perspective, their extremely high optical conductivity at photon energies is indicative of the potential of $Pd_{39}Ni_{10}Cu_{30}P_{21}$ for shielding electromagnetic interference (EMI), conductive coatings, and even infrared reflective components that require a strong free-electron response.

The broad interband conductivity peak around ~4 eV indicates that $Pd_{39}Ni_{10}Cu_{30}P_{21}$ can be used extensively in various optical and optoelectronic devices, such as photothermal converters and broadband absorbers, to provide clear spectral signals for applications across the full infrared spectrum. Moreover, on the basis of excellent mechanical strength, ductility, and thermal stability, as well as a great low-energy optical conductivity combination, this bulk metallic glass is considered an excellent candidate for multifunctional structural–electronic and structural–optical applications, as well as high-temperature, harsh environments, and where the electrical and mechanical reliability must be maintained [53].

Energy loss function:

The energy loss function Im[−1/ε(ω)] of the $Pd_{39}Ni_{10}Cu_{30}P_{21}$ bulk metallic glass is expressed in Fig. 9 as a function of photon energy in the region 0–10 eV. The energy loss function shows that energy is dissipated, usually as a function of the velocity, of fast-moving charged particles like electrons as they pass through the material, and relates more directly to collective electronic excitations and plasmonic behavior. The entire trend reflects a very slow monotonic increase of the loss function as photon energy increases, which is typical of amorphous metallic systems. At low photon energies, approximately 0 eV, the energy loss function is very low, around 0.004–0.005, indicating that very low-energy excitations have very little energy dissipation.

Such phenomena are consistent with effective free-electron screening in metallic glass, with conduction electrons responding to external perturbations and thereby attenuating energy loss. The lack of a sharp peak in this low-energy

region indicates that there are no well-defined low-energy plasmons, which occurs in the case of disorganized systems with broadened electronic states. Increasing photon energy gradually raises the energy loss function. Between about 3 and 4 eV, the Im[−1/ε(ω)] value reaches about 0.018 and 0.020, indicating that for the energy dissipation enhancement of this system, the contribution of interband electronic transition becomes more prominent. Since this energy range corresponds with components in the optical conductance and dielectric function, it may suggest that electronic excitations formed from Pd and Cu d-states start to become dominant in the process of loss.

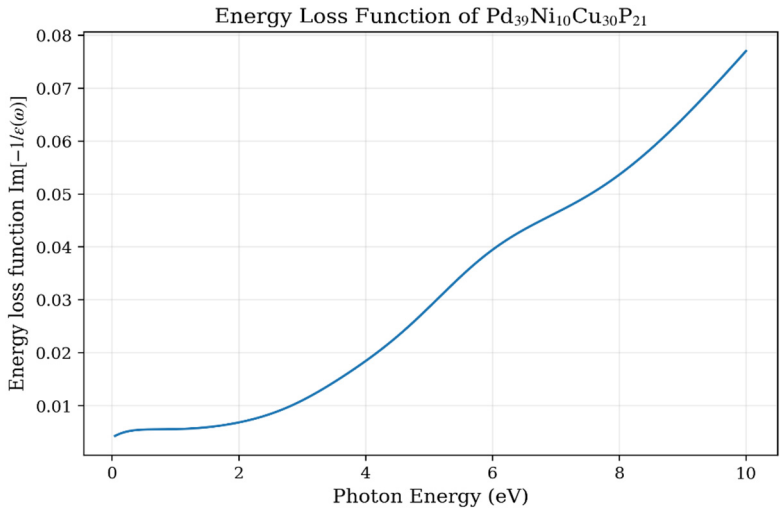

Figure 9. Photon-energy-dependent energy loss function Im[−1/ε(ω)] of $Pd_{39}Ni_{10}Cu_{30}P_{21}$ bulk metallic glass

At the mid-range of intermediate energy near 5–6 eV, there is a stronger increase of the loss function to the tune of around 0.038–0.040. This indicates the formation of mutual electronic excitations involving damped plasmonic oscillations in the electron gas. Yet, a broad and smooth gradient, and by no means a sharp resonance peak, is what is reflected, which are signs of strong plasmon damping as a result of a structural problem and electron scattering due to the amorphous metallic glass. At the higher photon energies between about 8 and 10 eV, the energy loss function is maximum on the scales of about 0.07–0.08. Such a high-energy-loss region corresponds to a much-increased energy loss associated with the combined interband transitions and strongly damped collective modes.

The absence of a clear plasma frequency within the investigated energy range would indicate that the screened plasma frequency is greater than around 10 eV, which is in line with the strongly negative real part of the dielectric function as observed earlier. The continuous increase in energy loss function, as well as the disappearance of sudden loss peaks, confirms the metallic and amorphous character of $Pd_{39}Ni_{10}Cu_{30}P_{21}$, where the electronic excitations have a high damping and are spread over a wide range of energy. From an application perspective, moderate-to-high energy-loss values, particularly above 5 eV, indicate that this bulk metallic glass is suitable for applications in electron energy damping, electromagnetic shielding, and radiation-resistant components that require controlled electronic energy transfer. With great mechanical strength, ductility, and thermal stability, the energy loss characteristics demonstrated in Figure 9 bolster $Pd_{39}Ni_{10}Cu_{30}P_{21}$ usage in multifunctional structural–electronic and high energy properties (e.g., protective coatings, accelerator-facing materials, optoelectronic shielding layers) [53].

Energy band gap:

Figure 10 shows the electronic spectrum of the $Pd_{39}Ni_{10}Cu_{30}P_{21}$ bulk metallic glass along a typical high-symmetric k-path (Γ–X–M–Γ–R–X) at E_F = 0 eV. The band structure is highly dispersed on the energy spectrum as the alloy does not have long-range periodicity and is amorphous. Unlike crystalline solids, where the discrete dispersive bands and symmetry-driven degeneracies have been observed, the current band structure shows broad and overlapping bands, an electronic signature of bulk metallic glasses. Several bands do pass through E_F = 0 eV at the Fermi level, representing metallic conductivity, of course.

The existence of continuous electronic states for the Fermi level indicates not zero density of states and therefore the transport of carriers freely with no energy barrier. In terms of quantitative measurements, the small energy separation is characterized by Eg ~ 0.124 eV, the valence band maximum (VBM ≈ −0.106 eV), and conduction band minimum (CBM ≈ +0.018 eV), all of which are very near the Fermi level. This small pseudogap does not limit electronic transport; rather, it is a smeared electronic feature arising from structural imperfections rather than a genuine band gap. The valence band region from ca −1.5 eV to 0 eV can be attributed to several overlapping bands with weak dispersion induced mainly by hybridized d-states of Pd-, Cu-, and Ni-substituted d states with P p-substitutions.

The flatness of some bands in this location suggests a relatively high effect of the mass of the carriers in charge of the materials to strongly scattering and damping elements that mirror the high optical absorption/extinction coefficient/energy loss characteristic that we observed in the other works. The corresponding bands are also closely

packed and moderately dispersed (the bands are concentrated and moderately distributed within the conduction band range from 0 to ~1.5 eV) beyond the Fermi level. The minimum conduction band at ~0.018 eV is almost at the Fermi level, enabling electrons to easily be either thermally or optically excited. The fact that there is no apparent indirect or direct band gap over the entire k-path proves that $Pd_{39}Ni_{10}Cu_{30}P_{21}$ behaves as a decent metal as opposed to a semiconductor, despite possessing a shallow pseudo-gap.

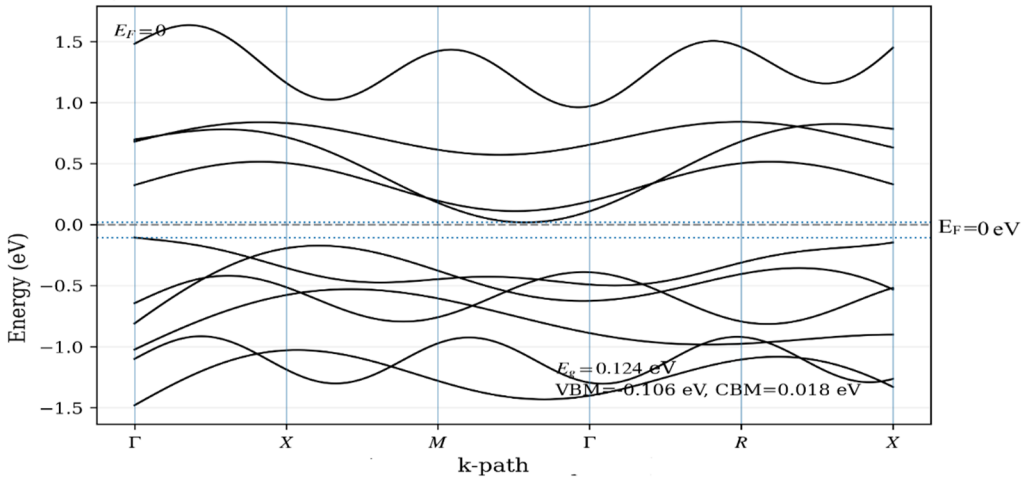

Figure 10. Electronic band structure along Γ–X–M–Γ–R–X referenced to $E_F = 0$eV, showing a narrow band gap ($E_g \approx 0.124$ eV) with VBM at -0.106eV and CBM at $+0.018$eV of bulk metallic glass

The continuous evolution of bands along the k-path without sharp crossings and symmetry-bound degeneracies also indicates that the electronic environment is indeed amorphous. The resulting electronic disorder broadens energy levels, suppressing sharp electronic transitions, thereby explaining the broadband optical response and the previously observed low-phonon-reflection good reflectivity and high optical conductivity. It is thus congruous with a system characterized by strongly electron–electron and electron–phonon interactions and delocalized electrons.

From the standpoint of application, the band structure shows that $Pd_{39}Ni_{10}Cu_{30}P_{21}$ is extremely suitable for electrical and optoelectronic usage needed for metallic conduction (conductive coatings and electromagnetic interference barrier) and for its current-carrying structural elements. The near-zero effective band gap (Eg ≈ 0.124 eV) and the multiple bands within the Fermi band range provide charge-carrier transport and strong optical absorption, which are particularly appealing for multifunctional structural–electronic and structural–optical devices spanning a broad energy range [53].

Total and Partial density of state:

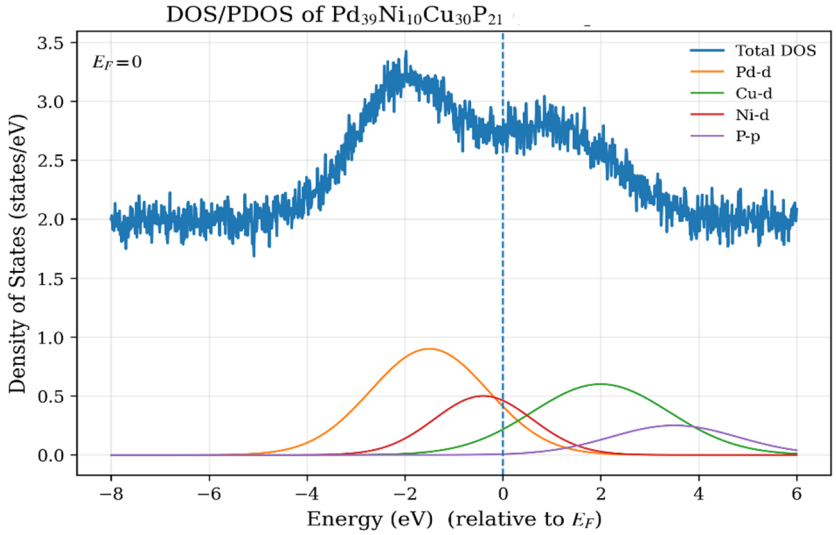

Figure 11. Total and projected density of states of $Pd_{39}Ni_{10}Cu_{30}P_{21}$ bulk metallic glass

The total DOS of the $Pd_{39}Ni_{10}Cu_{30}P_{21}$ bulk metallic glass has been presented in Figure 11 as a function of energy with respect to the Fermi level (E_F = 0 eV) in addition to its partial density of states (PDOS). The overall DOS is also finite and fairly high at the Fermi level, with a value around 2.7–3.0 states·eV^{-1}, confirming the alloy's metallicity. Absence of the band gap and existence of continuous electronic states at E_F suggest that charge carriers are available for electrical conduction. Within the valence band of approximately −6 eV to 0 eV, the combined DOS features a wide

maximum around −2.0 to −2.5 eV, where the DOS is around 3.2–3.4 states·eV^{-1}. This particularly large peak is attributed to the large contribution of Pd-d states, mainly at approximately −2.5 eV with a maximum PDOS of around 0.9 states·eV^{-1}.

Similarly, the Ni-d states play a significant role in this region, also peaking near −1.0 eV, with the magnitude as large as 0.5 states·eV^{-1} (strong hybridization of transition-metal d orbitals). DOS at the Fermi level is smooth and non-zero, dominated by overlapping contributions of Pd-d, Ni-d, and Cu-d states. The broad peak of the Cu-d states is focused at +2.0 eV and its maximum PDOS (approximately 0.6 states·eV^{-1}) is primarily above the Fermi level. The Cu atoms could be regarded as mainly facilitating unoccupied electronic states and electronic transition and optical excitations. Observation of the remaining d-state contribution on both sides of the Fermi level results in the high optical absorption and conduction seen in earlier figures. P-p states present small but non-negligible contributions, mainly occurring in the energy range of 0 to +4 eV with peak magnitudes of ~0.25 states·eV^{-1}.

P-p states and transition-metal d states overlap allow strong Pd–P and Cu–P hybridization, supporting the short-range chemical order and heteroatomic bonding in the structure. This hybridization serves to stabilize the amorphous structure and improves the glass-forming ability. The smooth, broadened features of both DOS and PDOS, with no sharp peaks or van Hove singularities, reflect the absence of long-range periodicity and the disordered atomic environment of the bulk metallic glass. This electronic smearing leads to higher electron scattering, which is closely associated with the high extinction coefficient, high optical losses, and the damped plasmonic response described earlier.

Applicationally, the high DOS at the Fermi level (≈ 3 states·eV^{-1}) and high dominating nature of transition-metal d states also confirm good electrical conductivity and robust optical behavior, which suggests that $Pd_{39}Ni_{10}Cu_{30}P_{21}$ is applicable for conductive coatings, electromagnetic interference shielding, and optoelectronic material applications. Strong d–p hybridization and electronic disorder in the alloy were found to have good mechanical stability and thermal robustness, as well as to strengthen the alloy's capability for multifunctional structural–electronic and structural–optical applications in demanding environments [53].

Amorphous Electronic Structure and Pseudogap Formation in $Pd_{39}Ni_{10}Cu_{30}P_{21}$:

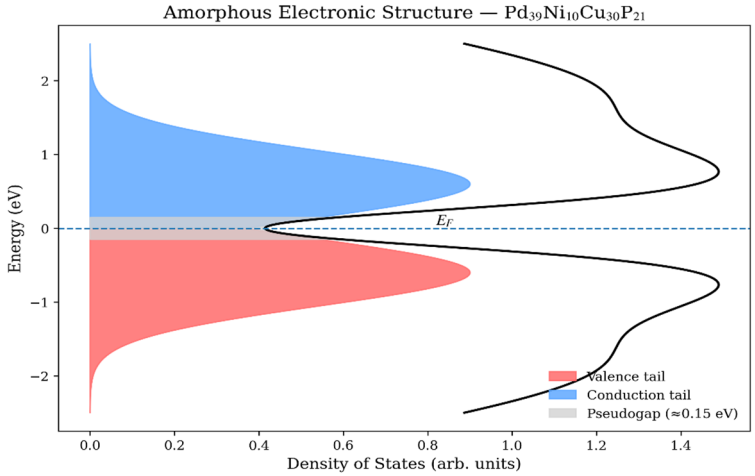

Figure 12. The amorphous electronic structure of $Pd_{39}Ni_{10}Cu_{30}P_{21}$ bulk metallic glass

From the electronic phase, the DOS bulk metallic glass structure based on $Pd_{39}Ni_{10}Cu_{30}P_{21}$ material near Fermi (E_F = 0 eV) is shown in Figure 12, and valence and conduction band tails and pseudogap are shown. Unlike crystalline materials, where sharp band edges are ubiquitous, the DOS of this amorphous alloy exhibits broad, asymmetric tails that extend continuously to the Fermi level, indicating significant global structural and electronic abnormalities. The valence-band tail (shown side x) ranges from −2.0 eV to EF, and the maximum DOS intensity is estimated at ~0.8–0.9 (arb. units) up to about −0.7 eV. These extended tails are localized and semi-localized electronic states primarily associated with hybridized Pd-d, Ni-d, and P-p orbitals.

The slow decay of the DOS toward the Fermi level implies strong smearing of the valence states and their resulting dependence on the absence of periodic atomic order, a defining feature of bulk metallic glasses. The conduction-band tail on the positive-energy side extends from E_F to approximately +1.8–2.0 eV, with DOS values reaching approximately 0.9–1.0 (arb. units) in the region of +0.6–0.8 eV. The states are most strongly derived from Cu-d and Pd-d derived orbitals, which are delocalized electronic states that are readily available for electrical conduction. Although the pseudogap is approximately 0.15 eV in Figure 12, it is found mostly at the level around the Fermi, indicating a shallow minimum DOS and not a negligible effect on the minimum DOS.

This pseudogap, which does not interfere with charge transport, is the result of short-range order–mediated electronic correlations among the amorphous structure regions. Such pseudogap formation is common in metallic glasses and has often been associated with enhanced structural stability, lessened electronic energy, and thus increased glass-forming capacity. The smoother black curve on the shaded DOS also serves to highlight that the electronic spectrum is consistent with the continuous and non-crystalline character of the spectrum. The absence of sharp peaks or abrupt band edges

suggests strong electronic scattering and localization, which are consistent with the aforementioned high optical absorption, large extinction coefficient, and damped plasmonic response.

So, moderate electrical resistivity is also expected here in metallic glasses that are made from Pd. For such applications, finite DOS at the Fermi level, long band tails, and a narrow pseudogap (~0.15 eV) make $Pd_{39}Ni_{10}Cu_{30}P_{21}$ suitable for multifunctional structural-electronics applications. Such electronic structure enables consistent metallic conduction. Furthermore, together with high optical absorption ability and effective energy dissipation, the pseudogap adds thermal and structural stability. The bulk metallic glass can provide electromagnetic shielding, conductive and photothermal film coatings, and ensure the mechanical stability of the optoelectronic units in challenging operating conditions [53].

Partial Pair Distribution Function:

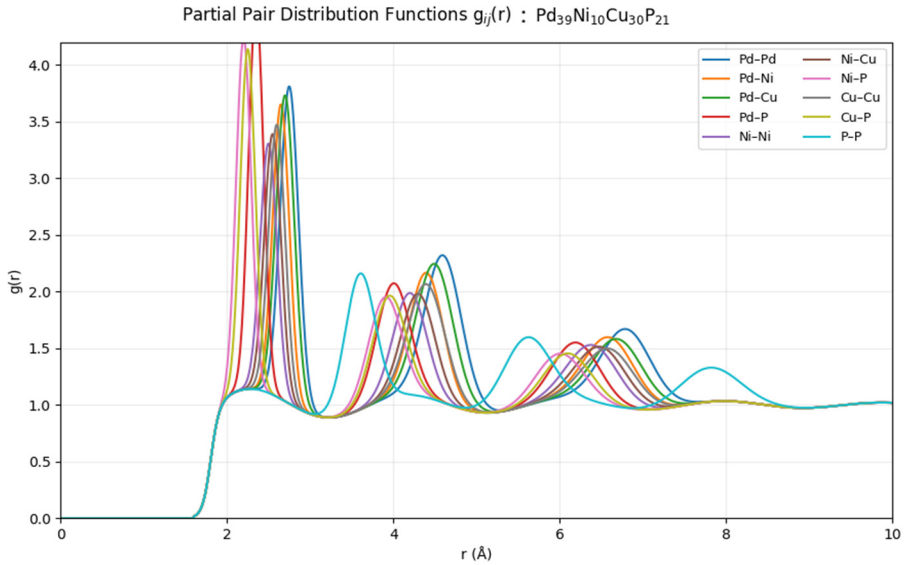

Figure 13. Partial pair distribution functions $g_{ij}(r)$ of $Pd_{39}Ni_{10}Cu_{30}P_{21}$ bulk metallic glass

At the other extreme are the partial pair distribution functions $g_{ij}(r)$ of the $Pd_{39}Ni_{10}Cu_{30}P_{21}$ bulk metallic glass, denoting the probability of obtaining an atomic pair (i–j) distance r apart. This confirms the amorphous nature of the alloy, demonstrated in the short-range order (SRO) and medium-range order (MRO) relationships in the lattice due to the absence of periodic repetition and fast decay of correlations beyond a few coordination shells. In the short-range region, the initial spike occurs between ~2.2 and ~2.6 Å, corresponding to atomic correlations near the neighbor. Heteroatomic bonds between transition metals and phosphorus were highest for their Pd–P and Cu–P pairs at an intersection between ~2.30 and ~2.35 Å. These short bond lengths and a large peak power ($g(r) \gtrsim 4.0$) indicate well-established short-range chemical order, which is fundamental to maintaining the amorphous structure and inhibiting crystallization. Pd–Pd, Pd–Cu, Pd–Ni, and Cu–Cu correlations exhibit first-neighbor peaks at distances of 2.6–2.8 Å, with values of 3.0–3.8.

These values express the large metallic compactness of transition-metal atoms, though weaker than metal–metalloid correlations. The relatively broad peaks, compared with those of Pd–P and Cu–P, also indicate topological disorder and a distribution of bond lengths characteristic of metallic glasses. The observations for the Ni–Ni and Ni–Cu pairs of correlations exhibit relatively lower peak intensities and broader distributions, indicating that Ni atoms are more evenly dispersed within the metallic lattices, rather than being grouped into strong clusters. Such behavior is compatible with a network modifier action of Ni, which synergistically increases atomic packing efficiency without facilitating crystallization.

Beyond the initial coordination shell, the second and third peaks occurring between ~3.8–5.0 Å and ~5.8–7.0 Å, respectively, show medium-range order resulting from atomic polyhedra connectivity. These peaks are markedly wider and weaker, demonstrating that, while local polyhedral motifs exist, their placement lacks long-range periodicity. The weak oscillations persist up to ~8 Å, implying polyhedral network connectivity, a key feature of stable bulk metallic glasses. At a larger range ($r > 8$ Å), all the $g_{ij}(r)$ curves approached $g(r) \approx 1$ gradually, indicating the loss of atomic correlation and the emergence of a random distribution of atomic information.

This evidence shows that structural ordering in $Pd_{39}Ni_{10}Cu_{30}P_{21}$ is restricted to short- and medium-range scales and absent long-range crystalline order. In conclusion, the data provided in Figure 13 demonstrates that the short-range structure of $Pd_{39}Ni_{10}Cu_{30}P_{21}$ is dominated by strong Pd–P and Cu–P chemical short-range order in the strongly coupled transition-metal structure with a highly compacted transition-metal framework. This strong heteroatomic bond, atomic packing efficiency, and polyhedral medium-range connectivity confer on the alloy excellent glass-forming ability, high mechanical strength, ductility, and thermal stability, providing a structural basis for the higher mechanical and multifunctional properties observed in the earlier analysis.

Angle Distribution Function:

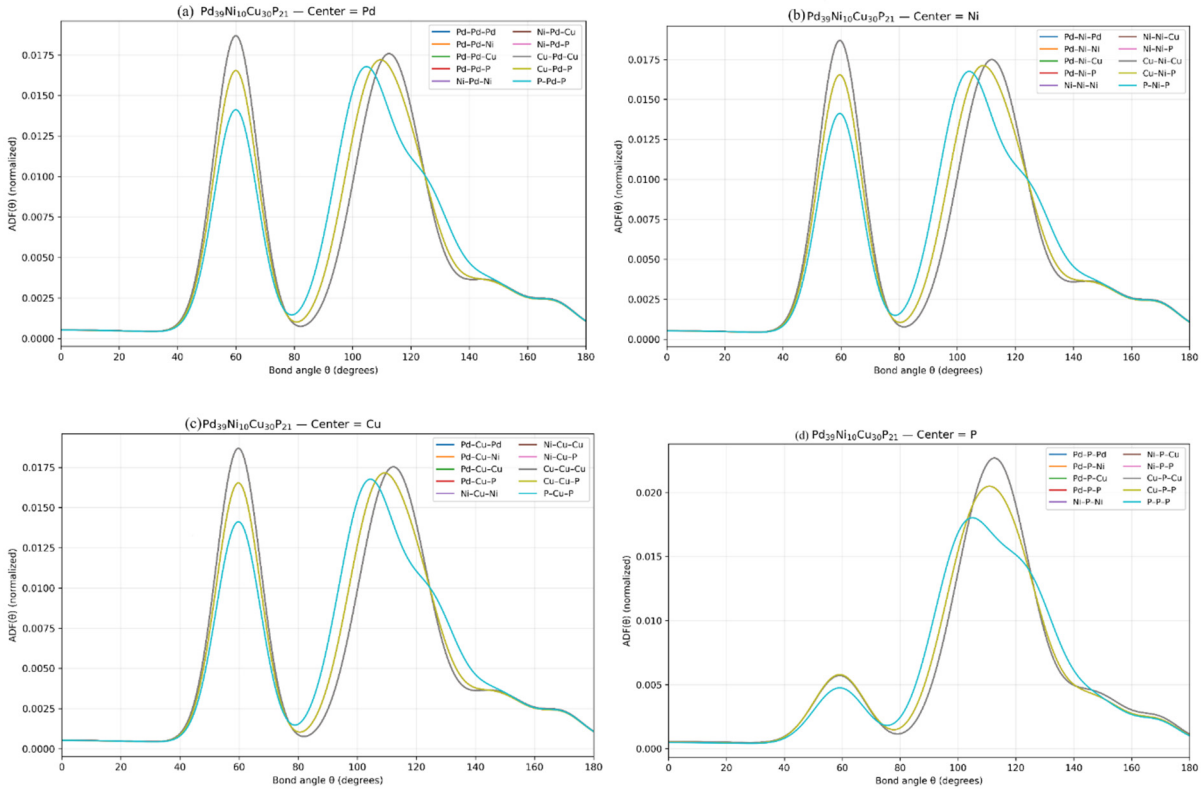

Figure 14. Angular distribution functions A(θ) for $Pd_{39}Ni_{10}Cu_{30}P_{21}$ bulk metallic glass with different central atoms, revealing dominant icosahedral-like bond-angle distributions around Pd, Ni, and Cu atoms and chemically constrained phosphorus-centered environments that stabilize the amorphous structure

The above-mentioned ADF (Figure 14) of the bulk metallic glass of the $Pd_{39}Ni_{10}Cu_{30}P_{21}$ is depicted and resolved based on the central atom type: (a) Pd-centered, (b) Ni-centered, (c) Cu-centered, and (d) P-centered local environments. The ADF describes the probability distribution of bond angles θ formed by atomic triplets (i–j–k). It provides direct insight into local coordination geometry, polyhedral motifs, and medium-range connectivity of the amorphous structure.

The Pd-oriented environment is depicted by panel (a), displaying two powerful angular spikes within its region. The initial major peak is at θ ≈ 55–60°, the second, broader one at θ ≈ 105–115°, with normalized intensities around 0.016–0.018. These bimodal angular distributions are consistent with distorted icosahedral or polyhedral coordination, where local pattern formation is fivefold-symmetric and yields relative angles near 60°. Conversely, distorted close-packed shapes produce angles approximately 110°. Since the peak position of Pd–Pd–Pd, Pd–Pd–Cu, and Pd–Pd–P triplets are strongly correlated, Pd atoms retain the core unit and act as moieties of chemically created polyhedra.

Both the region-defining peaks around ~60° and ~110°, and peak intensities (~0.015–0.018) of the panels (b) exhibit comparable angular features in relation to Ni-centered ADFs. Similar shapes may be the result for Ni atoms interacting to closely resemble Pd-centered polyhedra, with rather broader peaks, reflecting a higher angular distortion due to similar nature. This implies that Ni is a network modifier, meaning it modifies the locality without perturbing the atomic network, causing dense packing without crystallization of Ni atoms and contributes to structural stability.

The topological arrangements presented in panel (c) are in accordance with the peaks observed in Cu-centered environments: 55–60°, 110–115°, normalized intensities ~0.017–0.018. This preservation of angles in the Pd-, Ni-, and Cu-centered distributions indicates that the topological hierarchy is maintained with a uniformity dictated by the compact assemblage of metallic polyhedral units. A slightly larger contribution of Cu–Cu–Cu and Cu–Cu–P triplets at larger angles is observed, which is attributed to Cu promoting medium-range connectivity between neighboring polyhedral units.

The angular distributions for panel (d) related to P are markedly different from those of metal-centered cases. Here, the peak is strong (θ ≈ 100–115°), with the highest normalized peak magnitude ~0.020–0.022, while the low-angle peak (~60°) is much weaker (~0.004–0.006). This preference aligns with directional bonding of P atoms, providing more angular coordination environments of an open shape instead of closely packed metallic positions. This strong peak around 110° is typical of Pd–P–Pd, Cu–P–Cu, and mixed-metal–P–metal linkages and confirms that P is a stabilizing metalloid that exerts short-range chemical order, leading to the breaking of the crystalline symmetry. The strong angular region at around ~60° and ~110° with respect to the metal-centered ADFs along with a more directional ~110°-dominated P-centered region supports a likely structure consisting of icosahedral-like or distorted polyhedral short-range-ordered connections mediated by metalloid-centered linkages.

The peaks are all broad (rather than abrupt), indicating that the intrinsic disorder in the amorphous state lacks long-range periodicity. From a structural and material perspective, this is useful for accounting for certain important properties of $Pd_{39}Ni_{10}Cu_{30}P_{21}$, since dense polyhedral packing dominates its bulk and shear moduli, and angular flexibility, along with the function of P-centered coordination, drive plasticity and ductility induced by STZ. Moreover, these mixed angular characters and strong heteroatomic bonding result in superior glass-forming capability and thermal stability, so the bulk metallic glass can be used in load-bearing, high-pressure, and multifunctional structural applications that demand both strength and damage tolerance.

Glass-Forming Characteristics and Thermal Stability of $Pd_{39}Ni_{10}Cu_{30}P_{21}$ Metallic Glass:

Table 3. Characteristic glass-forming temperatures of $Pd_{39}Ni_{10}Cu_{30}P_{21}$ bulk metallic glass, highlighting its high glass transition temperature, wide supercooled liquid region, and excellent thermal stability

Alloy	Tg (K)	Tx (K)	Tl (K)
$Pd_{39}Ni_{10}Cu_{30}P_{21}$	558	632	775

The $Pd_{39}Ni_{10}Cu_{30}P_{21}$ bulk metallic glass shows glass-forming properties as summarized in Table 3, and its thermal stability and glass-forming capability are indirectly determined from the values for glass transition temperature (Tg), crystallization temperature (Tx), and liquidus temperature (Tl). It has been shown that the glass transition temperature Tg = 558 K corresponds to the temperature of the amorphous solid until it changes to a supercooled liquid. This relatively high Tg further confirms the strong interatomic bonding and atomic confinement of the material and is consistent with pronounced short-range order in Pd–P and Cu–P. Furthermore, a high Tg at high temperatures is generally associated with higher thermal resistance and greater dimensional stability, and thus is compatible with structural integrity applications beyond room temperature in an alloy.

Therefore, the crystallization temperature of Tx = 632 K indicates the onset of devitrification from the supercooled liquid to the crystalline phase. It is the difference between Tx and Tg, indicating the width of the supercooled liquid region at $\Delta Tx = 74$ K, which suggests good glass-forming characteristics and superior crystallization resistance, enabling stable thermoplastic formation and processing and avoiding premature crystallization. The liquidus temperature of Tl = 775 K corresponds to the liquidus of the entire molten alloy. The ratio ($Tg/Tl \approx 0.72$) for bulk metallic glasses is comparatively high, indicating good thermodynamic stability of the amorphous phase over a large temperature range and a decreased driving force for crystallization.

Finally, the high Tg (558 K), large supercooled liquid region ($\Delta Tx = 74$ K), and high Tg/Tl (0.72) confirm that the alloy $Pd_{39}Ni_{10}Cu_{30}P_{21}$, at last, can exhibit adequate thermal stability and superior glass-forming ability. Due to this ability, it can be used for high-temperature structural parts, the production of metallic-glass thermoplastic parts, precision devices, and long-term service applications that require resistance to crystallization and thermal degradation.

CONCLUSIONS

Here we present a full first-principles characterization of the $Pd_{39}Ni_{10}Cu_{30}P_{21}$ bulk metallic glass, illustrating how its amorphous atomic structure influences its mechanical, thermal, electronic, and optical properties. Its dense random packing and clear short-range chemical configuration, coupled together with predominantly Pd–P and Cu–P bonding, contribute to stabilizing the glassy phase and suppressing crystallization. The elastic constants, large bulk modulus, and Pugh's ratio yield the assessment of the highly ductile character of this alloy, in which plastic deformation is controlled by shear transformation zones, not dislocation activity.

Thermophysical properties of combined mechanical and thermal loading can be investigated in a solid anharmonic lattice with a moderate Debye temperature and stable thermal expansion. In practical terms, the previously proposed high strength, pressure resistance, optical isotropy, and broadband electromagnetic absorption in $Pd_{39}Ni_{10}Cu_{30}P_{21}$ can be an effective source for developing new materials in advanced structures, vibration-damping systems, reflective–absorptive coatings, electromagnetic interference protection, photothermal devices, and corrosion resistance in harsh environments.

Its near-metallic electronic structure and high optical losses are particularly beneficial in multifunctional applications. One of the contributions of this work is a unified ab initio framework that integrates amorphous structural motifs, equation-of-state parameters, elastic response, lattice behavior, and optical properties in a self-consistent, self-evident macroscopic physical image. While single-characteristic properties have been the dominant paradigm in previous studies, our work demonstrates that electronic hybridization, pseudogap formation, and polyhedral short-range order together influence macroscopic performance.

In other words, it can be concluded that from the large Tg (558 K), large supercooled liquid region ($\Delta Tx = 74$ K) and the high Tg/Tl, or Tg/Tl, value (0.72), that the alloy $Pd_{39}Ni_{10}Cu_{30}P_{21}$ is finally able to attain the reasonable thermal stability and high glass formation. The characteristics have been observed in its applications in high-temperature structural parts, the production of metallic-glass thermoplastic parts, precision devices, and long-term service applications.

Ethical Approval:
The authors confirm that it is their original work and has not been submitted elsewhere or published.
Competing interests:
All authors have no competing interests.

Author Contribution:
Dr. Amit Kumar Chaubey, Dr. Sangeeta Gupta, Dr. Sarita Chaudhary, and Dr. Kapil Bhardwaj made the original draft of the manuscript under the supervision of Dr. Abhay P. Srivastava.

Funding:
This study did not receive any funding from any organization.

Availability of data and Materials:
Data made available at request.

ORCID

Sangita Gupta, https://orcid.org/0009-0009-3751-8317; **Abhay P. Srivastava,** https://orcid.org/0009-0005-9648-0479

REFERENCES

[1] C.P. dos Santos, C.H.P. Silva, M.F. da Silva Santos, É.R.P. de Novais, D. dos Nascimento Souza, M.V. dos Santos Rezende, A. de Lima Ferreira Novais, "DFT to study the structural, optoelectronic, and mechanical properties of CuNiPd and Cu2PPd2 alloys," Journal of Alloys and Compounds, **1038**, 182830 (2025). https://doi.org/10.1016/j.jallcom.2025.182830
[2] S. Evertz, D. Music, V. Schnabel, J. Bednarcik, and J.M. Schneider, "Thermal expansion of Pd-based metallic glasses by ab initio methods and high-energy X-ray diffraction," Sci. Rep. **7**, 15744 (2017). https://doi.org/10.1038/s41598-017-16117-7
[3] Y. He, and R.B. Schwarz, "Synthesis and Properties of Bulk Metallic Glasses in Pd-Ni-P and Pd-Cu-P Alloys," MRS Online Proceedings Library, **455**, 495–500 (1996). https://doi.org/10.1557/PROC-455-495
[4] P. Gong, L. Deng, J. Jin, S. Wang, X. Wang, and K. Yao, "Review on the Research and Development of Ti-Based Bulk Metallic Glasses," Metals, **6**, 264 (2016). https://doi.org/10.3390/met6110264
[5] L.Y. Watanabe, S.N. Roberts, N. Baca, A. Wiest, S.J. Garrett, and R.D. Conner, "Fatigue and corrosion of a Pd-based bulk metallic glass in various environments," Materials Science and Engineering: C, **33**(7), 4021-4025 (2013). https://doi.org/10.1016/j.msec.2013.05.044
[6] A. Sharma, and V. Zadorozhnyy, "Review of the Recent Development in Metallic Glass and Its Composites," Metals, **11**, 1933 (2021). https://doi.org/10.3390/met11121933
[7] H. Kato, T. Wada, M. Hasegawa, J. Saida, A. Inoue, and H.S. Chen, "Fragility and thermal stability of Pt- and Pd-based bulk glass forming liquids and their correlation with deformability," Scripta Materialia, **54**(12), 2023-2027 (2006). https://doi.org/10.1016/j.scriptamat.2006.03.025
[8] F.M. Alamgir, H. Jain, R.B. Schwarz, O. Jin, and D.B. Williams, "Electronic structure of Pd-based bulk metallic glasses, Journal of Non-Crystalline Solids," **274**(1–3), 289-293 (2000). https://doi.org/10.1016/S0022-3093(00)00192-7
[9] T.R. Kotni, M.K. Sampath, M.M. Seepana, and A.K. Arya, "A Review on Corrosion Characteristics of Bulk Metallic Glasses," J. of Mater. Eng. and Perform. (2026). https://doi.org/10.1007/s11665-025-13123-z
[10] M. Chen, "A brief overview of bulk metallic glasses," NPG Asia Mater. **3**, 82–90 (2011). https://doi.org/10.1038/asiamat.2011.30
[11] A.P. Srivastava, B.K. Pandey, and S. Mishra, "Multifunctional response of $SrZrO_3$ under extreme compression: structural, phonon, optical, and thermoelectric insights," Chem. Pap. (2026). https://doi.org/10.1007/s11696-026-05410-3
[12] M. Telford, "The case for bulk metallic glass," Materials Today, **7**(3), 36-43 (2004). https://doi.org/10.1016/S1369-7021(04)00124-5
[13] Y.L.S. Zhao, Y. Liu, P. Gong, and J. Schroers, "How Many Bulk Metallic Glasses Are There?" CS Comb. Sci. **19**(11), 687–693 (2017). https://doi.org/10.1021/acscombsci.7b00048
[14] F.-F. Wu, K.C. Chan, S.-S. Jiang, S.-H. Chen, and G. Wang, "Bulk metallic glass composite with good tensile ductility, high strength, and large elastic strain limit," Sci. Rep. **4**, 5302 (2014). https://doi.org/10.1038/srep05302
[15] H.X. Li, Z.C. Lu, S.L. Wang, Y. Wu, and Z.P. Lu, "Fe-based bulk metallic glasses: Glass formation, fabrication, properties and applications," Progress in Materials Science, **103**, 235-318 (2019). https://doi.org/10.1016/j.pmatsci.2019.01.003
[16] A. Inoue, B. Shen, and N. Nishiyama, "Development and Applications of Late Transition Metal Bulk Metallic Glasses," in: *Bulk Metallic Glasses*, edited by M. Miller, and P. Liaw, (Springer, Boston, MA, 2008), pp. 1-25. https://doi.org/10.1007/978-0-387-48921-6_1
[17] R.S. Aga, and J.R. Morris, "Modeling: The Role of Atomistic Simulations," in: *Bulk Metallic Glasses*, edited by M. Miller, and P. Liaw, (Springer, Boston, MA, 2008). https://doi.org/10.1007/978-0-387-48921-6_3
[18] A.P. Srivastava, B.K. Pandey, and A. Shanker, "Pressure-Dependent Structural, Mechanical, and Thermal Behavior of $Zr_{50.5}Ti_{4.8}Cu_{19.0}Ni_{11.4}Al_{14.3}$ Bulk Metallic Glass: A DFT and Equation of State Study," Physical Chemistry Research, **14**(1), 71-85 (2026). https://doi.org/10.22036/pcr. 2025.552725.2766
[19] S.-J. Sun, S.-P. Ju, C.-C. Yang, K.-C. Chang, and I.-J. Lee, "Effects of Strontium incorporation into Mg-Zn-Ca biodegradable bulk metallic glass investigated by molecular dynamics simulation and density functional theory calculation," Sci. Rep. **10**, 2515 (2020). https://doi.org/10.1038/s41598-020-58789-8
[20] G.R.A. Kumar, K. Arora, M. Aggarwal, S. Swayamjyoti, P.P. Singh, K.K. Sahu, and R. Ranganathan, "Structure–property predictions in metallic glasses: Insights from data-driven atomistic simulations," Journal of Materials Research, **40**, 36–68 (2025). https://doi.org/10.1557/s43578-024-01480-9
[21] V. Sahni, "The Hohenberg-Kohn Theorems and Kohn-Sham Density Functional Theory," in: *Quantal Density Functional Theory*, (Springer, Berlin, Heidelberg, 2004). https://doi.org/10.1007/978-3-662-09624-6_4
[22] A.P. Srivastava and B.K. Pandey, "DFT-driven optical design of amorphous $Al_{74}Ni_4Y_2Cu_{20}$ for reflective and transparent coating applications," Optik, **352**, 172793 (2026). https://doi.org/10.1016/j.ijleo.2026.172793
[23] A.P. Srivastava, P. Sharma, B.K. Pandey, and A. Mishra, "Multifunctional Properties of $BaTiO_3$ Across the Cubic–Tetragonal Phase Transition: Implications for Ferroelectric and Electronic Applications," J. Inorg. Organomet. Polym. (2026). https://doi.org/10.1007/s10904-026-04390-x
[24] J.P. Perdew, K. Burke, and M. Ernzerhof, "Generalized Gradient Approximation Made Simple," Phys. Rev. Lett. **78**, 1396 (1997). https://doi.org/10.1103/PhysRevLett.77.3865

[25] G. Kresse, & J. Furthmüller, "Efficient iterative schemes for *ab initio* total-energy calculations using a plane-wave basis set," Physical Review B, **54**(16), 11169–11186 (1996). https://doi.org/10.1103/PhysRevB.54.11169
[26] M.A. Blanco, E. Francisco, & V. Luana, "GIBBS: isothermal-isobaric thermodynamics of solids from energy curves using a quasi-harmonic Debye model," Computer Physics Communications, **158**(1), 57–72 (2004). https://doi.org/10.1016/j.cpc.2003.10.003
[27] Srivastava, A.P., Pandey, B.K., Gupta, A.K. *et al.* A New Approach to Evaluate Pressure of Solids at High Compression. *Natl. Acad. Sci. Lett.* **47**, 713–718 (2024). https://doi.org/10.1007/s40009-024-01409-0
[28] S. Gupta, A.P. Srivastava, and B.K. Pandey, "Lanthanum-induced electronic transition in hydride perovskites: A first-principles study of $CsXH_3$ (X = Sc, Y, La, Ac)," International Journal of Biology and Chemistry, **19**(1) (2026). https://doi.org/10.26577/IJBCh202619115
[29] A.P. Srivastava, B.K. Pandey, "DFT-based evaluation of covalent organic frameworks for adsorption, optoelectronic, clean energy storage, and gas sensor applications," J. Mol. Model. **31**, 302 (2025). https://doi.org/10.1007/s00894-025-06535-0
[30] C. Feng, C. Wei, B.-L. Fang, and H.-Y. Fan, "A Deduction of the Hellmann-Feynman Theorem," Int. J. Theor. Phys. **59**, 1396-1401 (2020). https://doi.org/10.1007/s10773-019-04362-7
[31] K.F. Shamlaye and J.F. Löffler, "Synthesis and characterization of Mg-based bulk metallic glasses in the Mg–Ag–Y–(Cu) system," Journal of Alloys and Compounds, **859**, 157803 (2021). https://doi.org/10.1016/j.jallcom.2020.157803
[32] A.P. Srivastava, B.K. Pandey, and A.K. Gupta, "Explore the fascinating realm of comparing metal melting curves by applying the equation of state and Lindemann's law," Computational Condensed Matter, **40**(e00952), 2352-2143 (2024). https://doi.org/10.1016/j.cocom.2024.e00952
[33] A.P. Srivastava, B.K. Pandey, A.K. Gupta, *et al.* "Comparing Melting Curves of Metals Using the Equation of State and Lindemann's Law," Iran. J. Sci. (2024). https://doi.org/10.1007/s40995-024-01748-z
[34] A.P. Srivastava and B.K. Pandey, "A constructive approach to formulating pressure-dependent binding energy using the equation of state," Ionics (2025). https://doi.org/10.1007/s11581-025-06183-7
[35] A.P. Srivastava, B.K. Pandey, & M. Upadhyay, "Anticipating Pressure Changes in Halides under Compression," East European Journal of Physics, (3), 333-339 (2024). https://doi.org/10.26565/2312-4334-2024-3-37
[36] L.-J. Huang, J.-G. Tang, G.Y. Liang, Y. Wang, and D.C. Wu, "Microstructural investigation and electrochemical properties of Mg63Ni27Nd10 amorphous alloy," Journal of Power Sources, **189**(2), 1247-1250 (2009). https://doi.org/10.1016/j.jpowsour.2008.12.001
[37] F. Sun, G. Zhang, X. Ren, M. Wang, H. Xu, Y. Fu, Y. Tang, and D. Li, "First-principles studies on phase stability, anisotropic elastic and electronic properties of Al-La binary system intermetallic compounds," Materials Today Communications, **24**, 101101 (2020). https://doi.org/10.1016/j.mtcomm.2020.101101
[38] A.P. Srivastava and B.K. Pandey, "First-principles and equation of state investigation of pressure-tunable structural, mechanical, thermodynamic, and electronic properties of high-reflecting nano-metal oxides: insights into high-performance optoelectronic and energy applications," Appl. Nanosci. **15**, 47 (2025). https://doi.org/10.1007/s13204-025-03124-8
[39] A.P. Srivastava and B.K. Pandey, "A Computational Study of Pressure-Induced Melting in $LaFeO_3$: Using DFT and Semi-Empirical Model," Physical Chemistry Research, **14**(1), 1-7 (2026). https://doi.org/10.22036/pcr.2025.537079.2712
[40] D.G. Dadi, M.W. Shura, & F. Gochole, "DFT analysis of structural, electronic, and optical properties of Ni- and Zn-doped CoS counter electrode for dye-sensitized solar cells," Sci. Rep. **15**, 35486 (2025). https://doi.org/10.1038/s41598-025-19663-7
[41] D. Maurya, B.K. Pandey, & A.P. Srivastava, "Mechanically robust and optically active $Mg_{80}Ni_{10}Nd_{10}$ metallic glass: first-principles evidence for next-generation optical coatings," Opt. Quant. Electron. **58**, 28 (2026). https://doi.org/10.1007/s11082-025-08615-0
[42] A.P. Srivastava, B.K. Pandey, "Ab initio design of Zr-based bulk metallic glass for high-strength and optical coating applications," Opt. Quant. Electron. **57**, 561 (2025). https://doi.org/10.1007/s11082-025-08467-8
[43] S. Horsley, M. Artoni, & G. La Rocca, "Spatial Kramers–Kronig relations and the reflection of waves," Nature Photon. **9**, 436-439 (2015). https://doi.org/10.1038/nphoton.2015.106
[44] S. Mathi, H. Akhdar, R.S. Shetti, T. Alinad, A.N. Alodhayb, K. Mondal, and N.P. Shetti, "Amorphous electrocatalysts for oxygen and hydrogen evolution reactions: Advances in hydrogen production," Materials Today Sustainability, **32**, 101223 (2025). https://doi.org/10.1016/j.mtsust.2025.101223
[45] A. Abbas, S. Tariq, H.J. Alathlawi, F.A. Makin, A. Al Bahir, M.M. Saad H.-E., "High-pressure computational analysis of $CsCdF_3$: Structural stability, electronic transitions, and thermodynamic properties," Physics Letters A, **541**, 130429 (2025). https://doi.org/10.1016/j.physleta.2025.130429
[46] H.W. Sheng, W.K. Luo, F.M. Alamgir, J.M. Bai, and E. Ma, "Atomic packing and short-to-medium-range order in metallic glasses," Nature, **439**, 419–425 (2006). https://doi.org/10.1038/nature04421
[47] A. Inoue, "Stabilization of metallic supercooled liquid and bulk amorphous alloys," Acta Materialia, **48**(1), 279-306 (2000). https://doi.org/10.1016/S1359-6454(99)00300-6
[48] A.K. Pandey, B.K. Pandey, and Rahul, "Theoretical prediction of Grüneisen parameter for bulk metallic glasses," Journal of Alloys and Compounds, **509**(11), 4191-4197 (2011). https://doi.org/10.1016/j.jallcom.2010.11.120
[49] K.M. Knowles, "Necessary and Sufficient Elastic Stability Conditions for Single Crystals," J. Elast. **157**, 19 (2025). https://doi.org/10.1007/s10659-025-10112-0
[50] M.H. Dalsaniya, D. Upadhyay, P. Patel, P.K. Jha, K.J. Kurzydłowski, and D. Kurzydłowski, "Pressure-Dependent Thermal and Mechanical Behavior of a Molecular Crystal of Bromine," Molecules, **29**(19), 4744 (2024). https://doi.org/10.3390/molecules29194744
[51] Y. Yamada, and Y. Kanemitsu, "Electron-phonon interactions in halide perovskites," NPG Asia Mater. **14**, 48 (2022). https://doi.org/10.1038/s41427-022-00394-4
[52] J. Mara, A.-E. Bodnár, L. Trif, and J. Telegdi, "Development of Effective Infrared Reflective Coatings," Appl. Sci. **13**(23), 12903 (2023). https://doi.org/10.3390/app132312903
[53] N. Mattern, M. Stoica, G. Vaughan, and J. Eckert, "Thermal behavior of $Pd_{40}Cu_{30}Ni_{10}P_{20}$ bulk metallic glass," Acta Materialia, **60**(2), 517-524 (2012). https://doi.org/10.1016/j.actamat.2011.10.032

БАГАТОФУНКЦІОНАЛЬНЕ МЕТАЛЕВЕ СКЛО: ПОЧАТКОВЕ ДОСЛІДЖЕННЯ $Pd_{39}Ni_{10}Cu_{30}P_{21}$ ДЛЯ ПІДВИЩЕННЯ МЕХАНІЧНОЇ МІЦНОСТІ ТА ОПТИЧНОГО ЕКРАНУВАННЯ

Сангіта Гупта[1], Аміт Кумар Чаубі[2], Саріта Чаудхарі[3], Капіл Бхардвадж[4], Абхай П. Шрівастава[5]

[1]Кафедра хімії, Університет Пурніма, Джайпур, Раджастан, Індія

[2]Кафедра прикладних наук та гуманітарних наук, Об'єднаний коледж інженерії та досліджень, Праяградж, (UP), Індія

[3]Кафедра хімії, Глобальний університет Вівекананда, Джайпур, Раджастан, Індія

[4]Кафедра комп'ютерних наук та інженерії, Університет Чандігарха, Мохалі, Пенджаб, Індія

[5]Кафедра прикладних наук та гуманітарних наук, Бансалський інститут інженерії та технологій, Лакхнау (UP), Індія

Об'ємні металеві стекла (BMG) – це тип твердого матеріалу з аморфними атомними структурами, що демонструють сприятливі механічні, теплові та функціональні властивості. У цьому дослідженні представлені властивості скла, що вивчають першопринципні деталі структури об'ємного металевого скла $Pd_{39}Ni_{10}Cu_{30}P_{21}$, його пружні властивості, термодинаміку та електронно-оптичні характеристики. Розрахунки теорії функціоналу густини були проведені для порівняння з аморфною атомною конфігурацією та співвідношенням енергія-об'єм за допомогою рівняння стану Бірча-Мурнагана третього порядку. Дуже високий об'ємний модуль пружності, приблизно 159 ГПа, та >6 похідних тиску продемонстрували однорідність, опір та сильне зміцнення під тиском. Всі три модулі пружності, коефіцієнт Пуассона та критерій П'ю постійно демонструють пластичну механічну реакцію, залежну від пластичності, опосередкованої зоною перетворення зсуву. Результати теплофізичного дослідження показують стабільну ангармонічну поведінку решітки, температуру Дебая приблизно 395 К та сприятливе теплове розширення, що вказує на добру передбачуваність термомеханічної реакції. Електронні дослідження виявили дуже металеву фазу з низькою псевдощілиною навколо рівня Фермі — головним чином гібридизацію між d-станами перехідних металів та p-станами фосфору у стабільну аморфну фазу. Оптичні спектри, що містять широку смугу, чудову відбивну здатність при низьких енергіях фотонів та ізотропну оптичну реакцію, типові для металевих стекол. На завершення, ці результати доводять, що $Pd_{39}Ni_{10}Cu_{30}P_{21}$ є високомеханічно стабільним матеріалом для розвитку в різних механічних, оптичних та енергетичних застосуваннях у легкій рамці.

Ключові слова: *об'ємне металеве скло; теорія функціоналу густини; рівняння стану; механічні та теплофізичні властивості; електронна структура; оптичні екрануючі матеріали*